

Turbulence modeling over riblets via domain transformation

Mohammadamin Naseri and Armin Zare†

Department of Mechanical Engineering, University of Texas at Dallas, Richardson, TX 75080, USA

(Received xx; revised xx; accepted xx)

Numerical and experimental studies have demonstrated the drag-reducing potential of carefully designed streamwise-elongated riblets in lowering skin-friction drag. To support the systematic design of such surface corrugations, recent efforts have integrated simplified versions of the governing equations with innovative methods for representing the effects of rough boundaries on flow dynamics. Notably, the statistical response of the eddy-viscosity-enhanced linearized Navier-Stokes equations has been shown to effectively capture the ability of riblets in suppressing turbulence, quantify the influence of background turbulence on the mean velocity, and reproduce established drag-reduction trends. In this paper, we enhance the flexibility and computational efficiency of this simulation-free approach by implementing a domain transformation for surface representation, along with a perturbation analysis on a small geometric parameter of the riblets. While domain transformation complicates the differential equations, it provides accurate boundary representations and facilitates the analysis of complex riblet shapes at high Reynolds numbers by enabling perturbation analysis to simplify the dimensional complexity of the governing equations. Our method successfully predicts drag reduction trends for semi-circular riblets, consistent with existing literature. We further utilize our framework to investigate flow mechanisms influenced by riblets and extend our study to channel flows with friction Reynolds numbers up to 2003. Our findings reveal the emergence of Kelvin-Helmholtz rollers over large and sharp semi-circular riblets, contributing to the degradation of drag reduction in these geometries. Additionally, we examine the impact of riblets on near-wall flow structures, focusing on their suppression of streamwise-elongated structures in flows over large riblets.

Key words: drag reduction, turbulence control, turbulence modelling

1. Introduction

Skin friction accounts for approximately 45% of the total drag in aircraft transportation systems (Cousteix 1992). Additionally, surface roughness due to fouling increases total resistance by 23% for frigate-type hulls and 34% for very large crude carriers (Monty *et al.* 2016). Addressing skin-friction drag offers a substantial opportunity to reduce energy consumption and costs across the energy and transportation sectors. To harness this potential, numerous experimental (Walsh 1982; Walsh & Lindemann 1984; Bechert *et al.* 1997; Bechert, Bruse & Hage 2000) and numerical (Choi, Moin & Kim 1993; Goldstein, Handler & Sirovich 1995; García-Mayoral & Jiménez 2011*a*) studies have

† Email address for correspondence: armin.zare@utdallas.edu

demonstrated the drag-reducing advantages of streamwise-aligned, spanwise-periodic surface corrugations, commonly known as riblets. These investigations have identified a broad spectrum of drag reduction trends associated with the size and shape of riblets, paving the way for further optimization. Drag reduction achieved through riblets is attributed to their ability to regulate the spanwise movement of streamwise vortices in the near-wall region and to impede the downward transfer of momentum toward the wall by elevating vortices away from it (Choi *et al.* 1993; Suzuki & Kasagi 1994; Goldstein *et al.* 1995). This mechanism aligns with observations that riblets with spacing smaller than the diameter of near-wall streamwise vortices can prevent these vortices from settling into the riblet grooves (Lee & Lee 2001). Building on this understanding, earlier studies parameterize the drag-reducing behavior of riblets using metrics such as streamwise and spanwise protrusion heights (Bechert & Bartenwerfer 1989; Luchini, Manzo & Pozzi 1991; Ibrahim *et al.* 2021) and the roughness function (Orlandi & Leonardi 2006; Spalart & McLean 2011) in a linear viscous regime defined for small riblets. The decline in riblets' drag-reducing performance has been linked to the breakdown of this viscous regime (García-Mayoral & Jiménez 2011*b*), with numerous studies aiming to uncover geometric features of the surface that can describe the performance of riblets across both drag-reducing and drag-increasing regimes (e.g., von Deyn, Gatti & Frohnepfel (2022)).

1.1. Performance decline in large riblets

Several mechanisms have been proposed to explain the decline in drag reduction as riblet size increases. According to Choi *et al.* (1993), riblets with spacings $s^+ \approx 40$ allow streamwise vortices to lodge within their grooves, thereby exposing a larger surface area to turbulent flow. In contrast, riblets with smaller spacings suppress cross-flow in the near-wall region and push streamwise vortices away from the wall. In a complementary study, Suzuki & Kasagi (1994) conducted experiments demonstrating that a secondary flow develops near the tips of large riblets, enhancing turbulent momentum transport and reducing the effectiveness of the riblets. Similarly, the numerical study by Goldstein & Tuan (1998) attributed the drag increase to the formation of secondary streamwise vortices over widely spaced riblets, which induce additional stresses and inertial momentum transfer. Another mechanism proposed by García-Mayoral & Jiménez (2011*b*) suggests that large riblets trigger the formation of spanwise-coherent rollers near the corrugated surface due to a Kelvin-Helmholtz-like instability. This phenomenon has also been observed in flows over plant canopies (Finnigan 2000; Sharma & García-Mayoral 2020), as well as permeable (Jimenez *et al.* 2001) and porous walls (Breugem *et al.* 2006), and is attributed to localized transpiration or vertical momentum transport. García-Mayoral & Jiménez (2011*b*) showed that expressing riblet size in terms of the square root of the groove cross-sectional area, $l_g^+ = \sqrt{A_g^+}$, provides a universal drag-reduction curve for riblets of various sizes and shapes, with the optimal size occurring at $l_g^+ \approx 10.7$.

Recent studies have provided deeper insights into the emergence of the Kelvin-Helmholtz (K-H) instability in various riblet configurations. Endrikat *et al.* (2021) employed minimal-span channel simulations (MacDonald *et al.* 2017) to investigate this phenomenon, revealing its pronounced occurrence over large sharp triangular riblets. Rouhi *et al.* (2022) further demonstrated that K-H rollers forming over sharp triangular riblets can disrupt the Reynolds analogy, underscoring the instability's negative impact on drag reduction performance. Expanding on these findings, Endrikat *et al.* (2022) identified a redistribution of large-scale energy into smaller secondary flows in higher-speed flows over large two-scale trapezoidal riblets. This study, which combined boundary-layer hot-wire measurements with direct numerical simulations

(DNS) in minimal-span channels at higher flow speeds, introduced a generalized size parameter, which effectively collapses the drag curves for both single- and two-scale trapezoidal riblets. The coexistence of mechanisms contributing to drag increase with large riblets is highlighted by Modesti *et al.* (2021). They recognized the viscous-scaled groove width at the riblet mean height as a reliable indicator of whether the flow within the groove is governed by viscous or inertial effects. Vortices were observed to penetrate grooves wider than 20 viscous units, resulting in the emergence of secondary motions. However, this groove width threshold significantly exceeds the drag-reducing optimum for certain geometries, such as sharp triangular riblets or sharp semi-circular riblets examined in this study. For these types of riblet types, the inertial flow at the riblet crests was found to initiate the K-H instability, leading to a degradation in drag reduction performance (Modesti *et al.* 2021).

1.2. Prior model-based efforts in capturing the effects of riblets

Solving the governing equations with boundary conditions that account for riblet geometry requires a stretched mesh conforming to the surface. However, such an approach demands a high number of discretization points, imposing a computational cost that hinders its feasibility for design optimization and real-time decision-making in engineering applications. This challenge drives the development of low-complexity models that are capable of capturing the multi-scale nature of high-speed turbulent flows over periodic surface geometries. In this vein, recent efforts have focused on creating models that accurately represent the dynamics of flow around drag-reducing riblets, aiding their design and providing insights into the mechanisms behind drag increase in off-design conditions. For instance, Viggiano *et al.* (2024) assessed the onset of drag increase using the restricted nonlinear (RNL) and augmented RNL (ARNL) models to identify the prominent nonlinear interactions contributing to drag and to capture their effect with limited wavenumber pairs. Transpiration-resistance models that account for vertical momentum transport (Habibi Khorasani *et al.* 2022) and viscous vortex models that solve the Stokes-flow equations (Wong *et al.* 2024) are other examples that circumvent the need for DNS in predicting drag reduction for small to optimally sized riblets.

Systems-theoretic tools have also been applied to quantify the stochastic and harmonic responses of turbulent flows over riblets. Notably, the \mathcal{H}_2 norm of the linearized dynamics (Kasliwal, Duncan & Papachristodoulou 2012) and resolvent analysis (Chavarin & Luhar 2019) have been utilized to examine the receptivity of channel flows to corrugated surface geometry. Temporally periodic forcing of the linearized Navier-Stokes (NS) equations has also been employed to model the effect of periodic surfaces (Morgan & McKeon 2018; Huynh & McKeon 2020). Although these studies provide essential components for reduced-order models capable of receptivity analysis by creatively addressing rough boundary conditions, they fall short in accurately predicting skin-friction drag. Ran, Zare & Jovanović (2021) proposed a model-based framework for turbulence modeling in the presence of riblets, which explicitly accounted for harmonic interactions induced by the spatially periodic geometry. By incorporating the second-order statistics of flow fluctuations around riblets to adjust the turbulent eddy-viscosity near the rough surface, this framework demonstrated reliable drag predictions, even beyond the viscous regime.

A key factor in the effectiveness of reduced-order models for capturing the influence of riblets on flow is their approach to handling rough boundary conditions. Chavarin & Luhar (2019) and Ran *et al.* (2021) employed a volume penalization technique (Khadra *et al.* 2000) to approximate the effects of spatially periodic surfaces on turbulent flow. This method relies on a resistive function that represents the surface geometry as a static feedback term, penalizing the momentum equations within the roughness structure.

However, designing such resistive functions often requires parametric tuning, leading to approximate solutions. These solutions may fail to strictly adhere to no-penetration conditions at the riblet surface and do not provide a sharp representation of the immersed boundary (Fadlun *et al.* 2000). An alternative approach uses discrete forcing to impose boundary conditions directly on the immersed boundary. In this method, each cell adjacent to the fluid domain employs an interpolation scheme to implicitly incorporate the boundary conditions (Mittal & Iaccarino 2005). Since the interpolation procedure uses linearization to enforce the appropriate velocity at the first cell outside the boundary, the discrete forcing method requires a sufficiently fine grid near the boundary to maintain accuracy. Unlike volume penalization, discrete forcing is heavily tied to the specifics of the discretization scheme, making its implementation more complex. Moreover, imposing pressure boundary conditions on the immersed boundary involves solving a Poisson equation, which can introduce spurious pressure oscillations at the wall (Mittal *et al.* 2008; Verzicco 2023).

An effective approach to capturing the effects of corrugated boundaries is to transform the physical domain into a computational domain that incorporates the boundary geometry into the differential operators (Cabal, Szumbariski & Floryan 2002). For spatially periodic riblets, this transformation results in spatially periodic differential operators. Although this method complicates the governing equations, it allows for an accurate representation of the surface geometry. Previous studies have employed this technique to analyze the stability of channel flow over longitudinal riblets and to investigate transition mechanisms in the presence of riblets (Ehrenstein 1996; Kasliwal *et al.* 2012; Moradi & Floryan 2014). More recently, Jouin, Robinet & Cherubini (2024) employed the domain transformation method to perform both modal and non-modal stability analyses of transitional channel flow over riblets, demonstrating that riblets can induce an earlier laminar-turbulent transition through the formation of oblique waves.

1.3. *Preview of modeling framework and results*

In this paper, we complement the turbulence modeling framework of Ran *et al.* (2021) by introducing techniques that offer both flexibility and computational efficiency in capturing the effects of challenging roughness geometries in high-Reynolds-number flows. To model the impact of riblets on the flow, we adopt the domain transformation method proposed by Ehrenstein (1996). In the transformed domain, we follow Moarref & Jovanovic (2012); Ran *et al.* (2021) in capturing the influence of background turbulence on the mean velocity by relying on the statistical response of the eddy-viscosity-enhanced linearized Navier-Stokes equations. In Ran *et al.* (2021), the spatial periodicity of the resistive function induces numerous harmonic interactions in the fluctuation field, which can only be captured by a large state space whose analysis is computationally prohibitive. This issue is particularly exacerbated when analyzing high-speed flows over sharp riblets. We address this challenge in the transformed domain by treating the riblets height as a small parameter, enabling the use of perturbation analysis to efficiently compute second-order statistics of the linearized model. Using our simulation-free approach, we examine the effects of semi-circular riblets on kinetic energy and skin-friction drag in turbulent channel flow. The choice of semi-circular riblets, among other conventional riblet shapes, is driven by their superior durability compared to blade riblets and their more effective drag reduction compared to sawtooth riblets (Dean & Bhushan 2010). Our framework reliably predicts drag reduction trends reported by experimental and numerical studies (Bechert *et al.* 1997; García-Mayoral & Jiménez 2011*b*). It also allows us to study key turbulent flow mechanisms, including the K-H instability and near-wall cycle, in channel flow with Re_τ up to 2003 over large and sharp riblets.

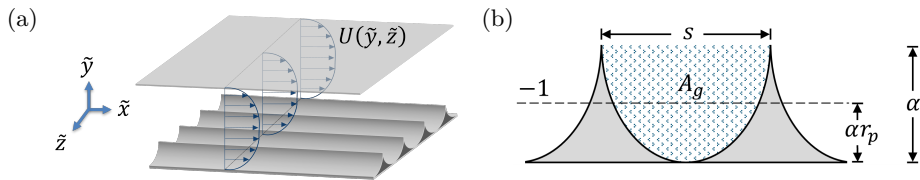


FIGURE 1. (a) Configuration of a channel flow with streamwise-constant spanwise-periodic riblets on the lower wall together with turbulent mean velocity profiles. (b) Semi-circular riblets of height α , peak to peak spacing $s = 2\pi/\omega_z$, and groove cross-sectional area A_g . The parameter r_p represents the proportion of the riblet height below $\tilde{y} = -1$.

1.4. Paper outline

The paper is organized as follows. In § 2, we formulate the problem, introduce the domain transformation to capture the shape of riblets, evaluate the mean flow in the transformed coordinates, and describe the necessity for studying the dynamics of velocity fluctuations. In § 3, we form the linearized eddy-viscosity-enhanced NS equations around the initial mean velocity profile and employ perturbation analysis to efficiently compute the second-order statistics of velocity fluctuations, which are then used to correct the turbulent viscosity and refine our predictions of the mean velocity and skin-friction drag. In § 4, we use our approach to capture the drag-reducing trends of semi-circular riblets in a turbulent channel flow. In § 5, we analyze the statistical response of the linearized dynamics to explain the degraded performance of large riblets at high Reynolds numbers. Finally, in § 6, we conclude with a summary of contributions and an outlook for future research directions.

2. Problem formulation

The incompressible NS and continuity equations governing the dynamics of turbulent flow within a channel that has longitudinal riblets mounted on its lower wall (figure 1(a)) are given by

$$\begin{aligned} \partial_t \tilde{\mathbf{u}} &= -(\tilde{\mathbf{u}} \cdot \tilde{\nabla}) \tilde{\mathbf{u}} - \tilde{\nabla} \tilde{P} + \frac{1}{Re_\tau} \tilde{\Delta} \tilde{\mathbf{u}}, \\ 0 &= \tilde{\nabla} \cdot \tilde{\mathbf{u}}, \end{aligned} \quad (2.1a)$$

subject to no-slip and no-penetration boundary conditions that respect the shape of the spanwise-periodic surface corrugation dictated by the shape function $r(\tilde{z}) > 0$, i.e.,

$$\tilde{\mathbf{u}}(\tilde{x}, \tilde{y} = 1, \tilde{z}, t) = 0, \quad \tilde{\mathbf{u}}(\tilde{x}, \tilde{y} = -1 + r(\tilde{z}), \tilde{z}, t) = 0. \quad (2.1b)$$

Here, \tilde{x} , \tilde{y} , and \tilde{z} denote the streamwise, wall-normal, and spanwise coordinates, respectively, t is time, $\tilde{\mathbf{u}}$ is the velocity vector, \tilde{P} is the pressure, $\tilde{\nabla}$ is the gradient, $\tilde{\Delta} = \tilde{\nabla} \cdot \tilde{\nabla}$ is the Laplacian, and $Re_\tau = u_\tau h / \nu$ is the friction Reynolds number defined in terms of the friction velocity $u_\tau = \sqrt{\tau_w / \rho}$, where τ_w is the wall-shear stress (averaged over horizontal directions and time) and ρ is the fluid density, h is the channel half height, and ν is the kinematic viscosity. In the governing equations, space is non-dimensionalized by h , velocity by u_τ , time by h/u_τ , and pressure by ρu_τ^2 . In this paper, we analyze the effect of riblets under constant-bulk conditions, in which the bulk flux remains constant via adjustment of the streamwise pressure gradient P_x .

In solving the NS equations subject to boundary conditions that capture the shape of riblets (equations (2.1)), multiple approaches have been offered to bypass the need for

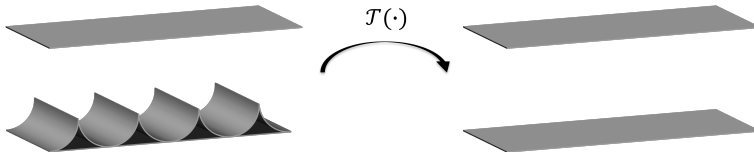


FIGURE 2. Schematic of the domain transformation $\mathcal{T}(\cdot)$ to translate the effect of spanwise periodic surface roughness onto the differential operators.

a stretched mesh that conforms to the surface geometry. Herein, we employ the domain transformation

$$x = \tilde{x}, \quad y = F(\tilde{y}, \tilde{z}), \quad z = \tilde{z}, \quad (2.2)$$

that maps the physical domain $(\tilde{x}, \tilde{y}, \tilde{z})$ where $\tilde{y} \in [-1 + r(\tilde{z}), 1]$ to a computational domain in which $y \in [-1, 1]$ (cf. figure 2). This is achieved using the mapping function

$$F(\tilde{y}, \tilde{z}) := \frac{2\tilde{y} - r(\tilde{z})}{2 - r(\tilde{z})}, \quad (2.3)$$

where $r(\tilde{z})$ can be any arbitrary streamwise-constant shape function that captures the geometry of the surface corrugation on the lower wall. For $2\pi/\omega_z$ -periodic semi-circular riblets studied in this paper, the shape function can be defined as

$$r(\tilde{z}) = \alpha \frac{\pi}{\omega_z} \left| \text{mod}\left(\tilde{z}, \frac{2\pi}{\omega_z}\right) \right|. \quad (2.4)$$

Here, $|\cdot|$ denotes the absolute value, α is the peak-to-trough height, and ω_z is spanwise frequency. To analyze the effect of riblets on drag, the riblet base is lowered by a proportion of the roughness height, i.e., αr_p with $r_p \in [0, 1]$, to ensure that the bulk flux matches that of a smooth channel flow of height 2; see figure 1(b). The choice of r_p also ensures the validity of our model when turbulence penetrates the riblet grooves, i.e., when riblets are larger than the optimal drag-reducing size, by assuming that the tip of riblets is located within the original channel (i.e., $\tilde{y} > -1$). The value of r_p is determined in an iterative manner to extend the original and transformed wall-normal domains to $\tilde{y} \in [-1 - \alpha r_p, 1]$ and $y \in [-1 - \alpha r_p, 1]$, respectively. The domain transformation reflects the surface geometry on the differential operators as

$$\begin{aligned} \partial_{\tilde{x}} &= \partial_x, & \partial_{\tilde{y}} &= F_{\tilde{y}} \partial_y, & \partial_{\tilde{z}} &= F_{\tilde{z}} \partial_y + \partial_z, \\ \partial_{\tilde{x}\tilde{x}} &= \partial_{xx}, & \partial_{\tilde{y}\tilde{y}} &= F_{\tilde{y}}^2 \partial_{yy}, & \partial_{\tilde{z}\tilde{z}} &= F_{\tilde{z}}^2 \partial_{yy} + 2F_{\tilde{z}} \partial_{yz} + \partial_{zz}, \end{aligned} \quad (2.5)$$

where $F_{\tilde{y}}$ and $F_{\tilde{z}}$ are the \tilde{y} and \tilde{z} derivatives of the mapping function (2.3), respectively.

While carefully designed small-size riblets have been shown to reduce drag and suppress the energy of the flow, large riblets are known for converse effects. This results in an *optimal* parameterization for conventional riblets (e.g., García-Mayoral & Jiménez (2011a)) that corresponds to the maximum achievable reduction in drag. In this paper, we not only analyze the effect of riblets on skin-friction drag and the turbulent kinetic energy, but also conduct a model-based analysis of previously identified flow mechanisms that not only deteriorate the drag-reducing capabilities of larger riblets, but can lead to an increase in skin-friction drag.

2.1. Mean flow equations

As skin-friction drag depends on the gradient of the turbulent mean velocity at the wall, a natural first step is to determine an approximation to the mean velocity in the

presence of riblets. By applying the Reynolds decomposition of the velocity field and pressure, i.e.,

$$\begin{aligned}\mathbf{u} &= \bar{\mathbf{u}} + \mathbf{v}, & \langle \mathbf{u} \rangle &= \bar{\mathbf{u}}, & \langle \mathbf{v} \rangle &= 0, \\ P &= \bar{P} + p, & \langle P \rangle &= \bar{P}, & \langle p \rangle &= 0,\end{aligned}\quad (2.6)$$

on the governing equations (2.1a), we arrive at the mean flow equations

$$\begin{aligned}\partial_t \bar{\mathbf{u}} &= -(\bar{\mathbf{u}} \cdot \nabla) \bar{\mathbf{u}} - \nabla \bar{P} + \frac{1}{Re_\tau} \Delta \bar{\mathbf{u}} - \nabla \cdot \langle \mathbf{v} \mathbf{v}^T \rangle, \\ 0 &= \nabla \cdot \bar{\mathbf{u}}.\end{aligned}\quad (2.7)$$

Here, $\bar{\mathbf{u}} = [U \ V \ W]^T$ is the vector of mean velocity components, $\mathbf{v} = [u \ v \ w]^T$ is the vector of velocity fluctuations around $\bar{\mathbf{u}}$, p is the fluctuating pressure around the mean \bar{P} , $\langle \cdot \rangle$ denotes the expected value,

$$\langle \mathbf{u}(x, y, z, t) \rangle = \lim_{T \rightarrow \infty} \frac{1}{T} \int_0^T \mathbf{u}(x, y, z, t + \tau) d\tau, \quad (2.8)$$

and ∇ and Δ are the gradient and Laplacian that take the following form by virtue of the domain transformation (2.2):

$$\nabla = [\partial_x, F_{\tilde{y}} \partial_y, F_{\tilde{z}} \partial_y + \partial_z]^T, \quad \Delta = \partial_{xx} + F_{\tilde{y}}^2 \partial_{yy} + F_{\tilde{z}}^2 \partial_{yy} + 2F_{\tilde{z}} \partial_{yz} + \partial_{zz}.$$

In equations (2.7), the Reynolds stress tensor $\langle \mathbf{v} \mathbf{v}^T \rangle$ captures the effect of background turbulence by quantifying momentum transport due to turbulent fluctuations (McComb 1991), but is unknown. In the absence of a fully determined stress-tensor, the mean flow equations are not closed and cannot be solved without adopting a turbulence model. To overcome the closure problem, we employ the turbulent viscosity hypothesis (McComb 1991) and assume turbulent momentum to be transported in the direction of the mean rate of strain, i.e.,

$$\langle \overline{\mathbf{v} \mathbf{v}^T} \rangle - \frac{1}{3} \text{trace}(\langle \overline{\mathbf{v} \mathbf{v}^T} \rangle) I = -\frac{\nu_T}{Re_\tau} (\nabla \bar{\mathbf{u}} + (\nabla \bar{\mathbf{u}})^T). \quad (2.9)$$

Here, overline indicates averaging over horizontal dimensions, I is the identity operator, and $\nu_T(y)$ is the turbulent eddy viscosity normalized by molecular viscosity. Incorporating the turbulent viscosity hypothesis (2.9) into equations (2.7) yields

$$\begin{aligned}\partial_t \bar{\mathbf{u}} &= -(\bar{\mathbf{u}} \cdot \nabla) \bar{\mathbf{u}} - \nabla \bar{P} + \frac{1}{Re_\tau} \nabla \cdot ((1 + \nu_T) (\nabla \bar{\mathbf{u}} + (\nabla \bar{\mathbf{u}})^T)), \\ 0 &= \nabla \cdot \bar{\mathbf{u}}.\end{aligned}\quad (2.10)$$

After applying the domain transformation (2.2), the steady-state solution to the nonlinear mean flow equations (2.10) can be obtained using Newton's method to only contain a streamwise velocity component, i.e., $\bar{\mathbf{u}} = [U(y, z) \ 0 \ 0]^T$, which solves the linear equation

$$(1 + \nu_T) [F_{\tilde{y}}^2 U_{yy} + F_{\tilde{z}}^2 U_{yy} + 2F_{\tilde{z}} U_{yz} + U_{zz}] + F_{\tilde{y}}^2 \nu_T' U_y = Re_\tau \bar{P}_x \quad (2.11)$$

Here, ν_T' is the wall-normal derivative of ν_T , and the mean velocity $U(y, z)$ obeys no-slip boundary conditions on both walls by virtue of the domain transformation. Due to the periodic geometry of riblets, a harmonic expansion of the mapping function $F(\tilde{y}, \tilde{z})$ (equation (2.3)) in the spanwise direction, i.e.,

$$F(\tilde{y}, \tilde{z}) = \sum_{m=-\infty}^{\infty} F_m(\tilde{y}) e^{im\omega_z \tilde{z}}, \quad (2.12)$$

warrants the parameterization of equation (2.11) and its solution U over the spanwise frequency of riblets, ω_z , i.e.,

$$U(y, z) = \sum_{k=-\infty}^{\infty} U_k(y) e^{ik\omega_z z}. \quad (2.13)$$

Substituting expansions (2.12) and (2.13) into equation (2.11) yields the equation for the k th harmonic $U_k(y)$ as

$$\underbrace{\left[(1 + \nu_T) \left((F_{\tilde{y},0}^2 + F_{\tilde{z},0}^2) \partial_{yy} + 2F_{\tilde{z},0} \partial_{yz} + \partial_{zz} \right) + \nu'_T F_{\tilde{y},0}^2 \partial_y \right]}_{\mathbf{L}_{k,0}} U_k + \underbrace{\sum_{m=-\infty \setminus \{0\}}^k [\nu'_T F_{\tilde{y},m}^2 \partial_y]}_{\dots} \dots + \underbrace{\left[(1 + \nu_T) \left((F_{\tilde{y},m}^2 + F_{\tilde{z},m}^2) \partial_{yy} + 2(k-m)F_{\tilde{z},m} \partial_{yz} \right) \right]}_{\mathbf{L}_{k,m}} U_{k-m} = \begin{cases} Re_\tau \bar{P}_x, & k = 0 \\ 0, & k \neq 0 \end{cases}$$

which can be brought into the bi-infinite matrix form

$$\begin{bmatrix} \ddots & & & & & \\ & \ddots & & & & \\ & & \mathbf{L}_{-1,0} & \mathbf{L}_{-1,1} & \mathbf{L}_{-1,2} & \ddots \\ & & \mathbf{L}_{0,-1} & \mathbf{L}_{0,0} & \mathbf{L}_{0,1} & \ddots \\ & & \mathbf{L}_{1,-1} & \mathbf{L}_{1,0} & \mathbf{L}_{1,1} & \ddots \\ & & & & & \ddots \end{bmatrix} \begin{bmatrix} \vdots \\ U_{-1} \\ U_0 \\ U_1 \\ \vdots \end{bmatrix} = \begin{bmatrix} \vdots \\ 0 \\ Re_\tau \bar{P}_x \\ 0 \\ \vdots \end{bmatrix}. \quad (2.14)$$

Depending on the significance of higher-order harmonics in the Fourier expansion of F (equation (2.12)), the bi-infinite matrices and vectors can be truncated to account for a finite number of harmonic that provide a good approximation to the solution of equation (2.11).

The flow in the vicinity of the solid surface is dominated by viscosity, and can therefore, be assumed laminar within the grooves of riblets (García-Mayoral & Jiménez 2011a). Because of this, we consider $\nu_T = 0$ for $\tilde{y} \leq -1$ (cf. figure 1(b)). On the other hand, a well defined turbulent viscosity ν_T is needed for $\tilde{y} > -1$, which of course, is not easy to come by as it depends on the velocity fluctuations around the turbulent mean U . A good starting point may be provided by the turbulent viscosity profile that obtains the turbulent mean velocity in channel flow over smooth walls. The analytical expression for one such turbulent viscosity profile is given by (Reynolds & Tiederman 1967)

$$\nu_{T_0}(y) = \frac{1}{2} \left(\left(1 + \left(\frac{c_1}{3} Re_\tau (1 - y^2)(1 + 2y^2)(1 - e^{-(1-|y|)Re_\tau/c_2}) \right)^2 \right)^{1/2} - 1 \right), \quad (2.15)$$

which is obtained from extending the model introduced by Cess for pipe flow (Cess 1958) to the channel flow. In this model, parameters c_1 and c_2 are selected to minimize the least squares deviation between the mean streamwise velocity obtained in experiments and simulations and the steady-state solution to the mean flow equations using the averaged wall-shear stress $\tau_w = 1$. For channel flow with $Re_\tau = 186$, $c_1 = 0.61$ and $c_2 = 46.2$ provide the best fit to the turbulent mean velocity resulting from the DNS of Del Álamo & Jiménez (2003). Given the aforementioned parameterization for ν_T , we can solve equation (2.14) using block operators (Aurentz & Trefethen 2017) that divide the wall-normal extent of the computational domain into upper turbulent and lower laminar regions. In this case, smoothness would be enforced at the intersection of these

regions via interface conditions,

$$\begin{aligned} U_k(y = -1^+, z) &= U_k(y = -1^-, z), \\ \frac{\partial U_k}{\partial y}(y = -1^+, z) &= \frac{\partial U_k}{\partial y}(y = -1^-, z) \end{aligned}$$

for all k . Figure 3(a) shows the solution to equation (2.11) for a turbulent channel flow with $Re_\tau = 186$ subject to $\bar{P}_x = -1$ over semi-circular riblets with $\alpha/s = 0.87$, $\omega_z = 60$, and $r_p = 0.487$. Here, we use a pseudospectral scheme with Chebyshev polynomials (Weideman & Reddy 2000) with $N_t = 140$ and $N_b = 30$ collocation points to discretize the top ($y \in [-1, 1]$) and bottom ($y \in [-1 - \alpha r_p, -1]$) portions of the wall-normal dimension, respectively, and 25 harmonics were used to capture the spanwise-periodic shape of the riblets, i.e., $m \in [-12, 12]$ in the Fourier expansion of $F(\tilde{y}, \tilde{z})$ (equation (2.12)).

2.2. Skin-friction drag reduction

In the presence of riblets, skin-friction drag at the lower wall, D , can be computed using the slope of the mean velocity at the upper wall,

$$D = \bar{P}_x - \frac{\omega_z}{2\pi} \int_0^{2\pi/\omega_z} \frac{\partial U}{\partial y}(y = 1, z) dz \quad (2.16)$$

where $\bar{P}_x = -D_s/Re_\tau$, with D_s denoting the slope of the mean velocity at the wall in the absence of riblets. It is evident that the mean velocity in figure 3(a) respects the shape of the riblets. However, a parametric study over riblets with $\alpha/s = 0.87$ but with different frequencies ω_z fails to capture any drag reduction and provides no optimal spacing that maximizes drag reduction (figure 3(b)). What's more, the resulting drag reduction does not follow commonly reported trends from prior numerical and experimental studies (see, e.g., Bechert *et al.* (1997); García-Mayoral & Jiménez (2011*b*)). While the turbulent viscosity hypothesis provides an opportunity for closing the mean flow equations, the choice of an appropriate turbulent eddy-viscosity ν_T that captures the effect of riblets on the background turbulence challenges our analysis. To address this issue, we adopt the iterative procedure of Moarref & Jovanovic (2012); Ran *et al.* (2021) in starting from the turbulent viscosity over smooth surfaces and utilizing the dynamics of velocity fluctuations \mathbf{v} to correct this initial profile.

3. Turbulence modeling in channel flow over riblets

In this section, we follow the turbulence modeling framework of Moarref & Jovanovic (2012) in determining a turbulent viscosity ν_T that enables an accurate prediction of skin-friction drag in channel flow over riblets. As highlighted below, this is done through a sequence of steps whereby modifications are introduced to ν_{T_0} , i.e., the turbulent viscosity of a smooth channel flow. The model-based framework involves the following steps:

(i) A turbulent mean velocity profile is obtained by solving equation (2.11), where closure is achieved using turbulent viscosity ν_{T_0} in equation (2.15).

(ii) The linearized NS equations around the mean flow obtained in step (i) are used to compute the second-order statistics of the velocity field and provide a modification to ν_{T_0} based on a model we adopt for turbulent viscosity in § 3.1.

(iii) The modified turbulent viscosity is used to correct the mean velocity and compute skin-friction drag.

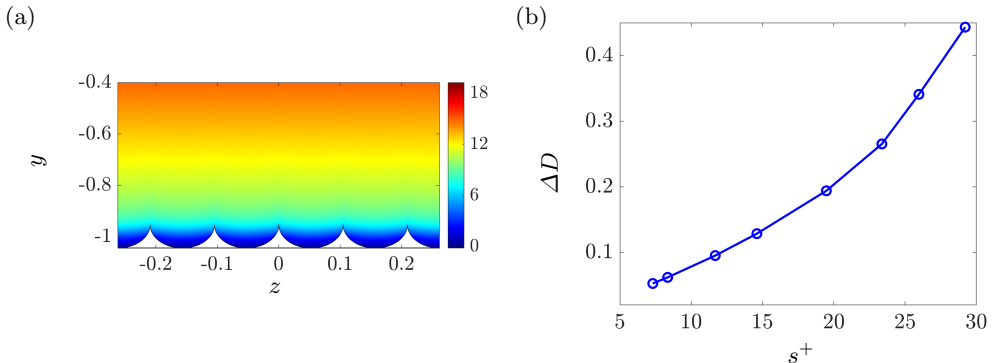


FIGURE 3. (a) The streamwise mean velocity $U(y, z)$ for turbulent channel flow with $Re_\tau = 186$ over semi-circular riblets of $\alpha/s = 0.87$ and $\omega_z = 60$; (b) The relative drag reduction $\Delta D := (D - D_s)/D_s$ computed using the solution to equation (2.11) with $\nu_T = \nu_{T0}$.

As argued in Ran *et al.* (2021), the separation of steps (i) and (iii) is justified by the slower time evolution of the mean compared to the fluctuating component whose second-order statistics are used to correct it. In § 4, we show that the modification to the mean velocity results in an accurate prediction of drag in the presence of semi-circular riblets. Furthermore, in § 5 we use the statistical signature of the flow obtained in step (ii) to examine the physical mechanisms affecting skin-friction drag in the presence of sharp riblets of different size.

3.1. Turbulent viscosity model

If k/ϵ and $k^{3/2}/\epsilon$ are chosen as time and length scales, turbulent viscosity can be expressed as (Pope 2000, Chapter 10)

$$\nu_T = c Re_\tau^2 \frac{k^2}{\epsilon}, \quad (3.1)$$

where k and ϵ are the turbulent kinetic energy and its rate of dissipation, respectively, and $c = 0.09$ is an established multiplicative constant for the near-wall region (Pope 2000). The kinetic energy and its rate of dissipation can be determined from second-order velocity statistics as

$$\begin{aligned} k(y) &= \frac{1}{2} (\langle \overline{u u} \rangle + \langle \overline{v v} \rangle + \langle \overline{w w} \rangle), \\ \epsilon(y) &= 2 (\langle \overline{u_x u_x} \rangle + \langle \overline{v_y v_y} \rangle + \langle \overline{w_z w_z} \rangle + \langle \overline{u_y v_x} \rangle + \langle \overline{u_z w_x} \rangle + \langle \overline{v_z w_y} \rangle) \\ &\quad + \langle \overline{u_y u_y} \rangle + \langle \overline{w_y w_y} \rangle + \langle \overline{v_x v_x} \rangle + \langle \overline{w_x w_x} \rangle + \langle \overline{u_z u_z} \rangle + \langle \overline{v_z v_z} \rangle. \end{aligned} \quad (3.2)$$

The widely used $k - \epsilon$ model (Jones & Launder 1972; Launder & Sharma 1974) provides differential transport equations for k and ϵ , but is computationally demanding. An alternative simulation-free way of approximating these quantities is to compute them from the second-order statistics of the linearized flow dynamics around the mean velocity.

3.2. Stochastically forced linearized Navier-Stokes equations

By linearizing the NS equations (2.1a) around the mean velocity $\bar{\mathbf{u}} = [U(y, z) \ 0 \ 0]^T$ obtained from solving equation (2.11) and \bar{P} , we arrive at the dynamics of velocity

fluctuations

$$\begin{aligned}\partial_t \mathbf{v} &= -(\nabla \cdot \bar{\mathbf{u}}) \mathbf{v} - (\nabla \cdot \mathbf{v}) \bar{\mathbf{u}} - \nabla p + \frac{1}{Re_\tau} \nabla \cdot ((1 + \nu_T)(\nabla \mathbf{v} + (\nabla \mathbf{v})^T)) + \mathbf{f} \\ 0 &= \nabla \cdot \mathbf{v}.\end{aligned}\tag{3.3}$$

In these so called eddy-viscosity-enhanced linearized NS equations, molecular viscosity is augmented by turbulent viscosity ν_T to compensate for the nonlinear terms that are dropped through linearization (Reynolds & Hussain 1972; Del Álamo & Jiménez 2006; Pujals *et al.* 2009; Hwang & Cossu 2010; Jovanovic 2020; Abootorabi & Zare 2023) and \mathbf{f} is a zero-mean white-in-time stochastic forcing that excites the stochastic response of the linearized dynamics. Due to the domain transformation (2.2), the boundary conditions for equations (3.3) are given by $\mathbf{v}(x, y = \pm 1, z, t) = 0$ and the $2\pi/\omega_z$ periodicity of the surface is instead reflected onto the differential operators. As a result, in contrast to the smooth channel flow, the normal mode in the spanwise direction is no longer given by $e^{ik_z z}$; the normal modes in the spatially periodic direction are given by Bloch waves (Odeh & Keller 1964; Bensoussan, Lions & Papanicolaou 1978), resulting in the wavenumber parameterization

$$\mathbf{v}(x, y, z, t) = e^{ik_x x} e^{i\theta z} \hat{\mathbf{v}}_\theta(k_x, y, z, t)$$

with $\theta \in [0, \omega_z)$ for velocity fluctuations and all other quantities in equation (3.3). Here, $k_x \in \mathbb{R}$ is the streamwise wavenumber and $\hat{\mathbf{v}}_\theta(k_x, y, z, t)$ is a $2\pi/\omega_z$ -periodic function in the spanwise direction with Fourier series expansion

$$\hat{\mathbf{v}}_\theta(k_x, y, z, t) = \sum_{n \in \mathbb{Z}} \hat{\mathbf{v}}_n(k_x, y, \theta, t) e^{in\omega_z z}.\tag{3.4}$$

In this expansion, $\{\hat{\mathbf{v}}_n(k_x, y, \theta, t)\}_{n \in \mathbb{Z}}$ are the coefficients of the Fourier series expansion of $\hat{\mathbf{v}}_\theta(k_x, y, z, t)$. Based on this,

$$\mathbf{v}(x, y, z, t) = \sum_{n \in \mathbb{Z}} \hat{\mathbf{v}}_n(k_x, y, \theta, t) e^{i(k_x x + \theta_n z)},\tag{3.5}$$

where $\theta_n = \theta + n\omega_z$ is the spanwise wavenumber. By substituting (3.5) into the linearized dynamics (3.3) and eliminating pressure through a standard conversion (Schmid & Henningson 2001), the differential equations for the dynamics of \mathbf{v} can be brought into the evolution form

$$\begin{aligned}\partial_t \boldsymbol{\psi}_\theta(k_x, y, t) &= [\mathcal{A}_\theta(k_x) \boldsymbol{\psi}_\theta(k_x, \cdot, t)](y) + \mathcal{B}_\theta(k_x) \mathbf{f}_\theta(k_x, y, t), \\ \mathbf{v}_\theta(k_x, y, t) &= [\mathcal{C}_\theta(k_x) \boldsymbol{\psi}_\theta(k_x, \cdot, t)](y),\end{aligned}\tag{3.6}$$

in which the state vector $\boldsymbol{\psi}$ consists of the wall-normal velocity v and vorticity $\boldsymbol{\eta} = \partial_z u - \partial_x w$. Here, $\boldsymbol{\psi}_\theta$, \mathbf{v}_θ , and \mathbf{f}_θ are bi-infinite column vectors parameterized by the streamwise wavenumber k_x and the spanwise wavenumber offset θ , e.g., for each (k_x, θ) pair, $\boldsymbol{\psi}_\theta(k_x, y, t) = \text{col} \left\{ \hat{\boldsymbol{\psi}}_n(k_x, y, \theta, t) \right\}_{n \in \mathbb{Z}}$ with $\hat{\boldsymbol{\psi}}_n = [\hat{v}_n \ \hat{\boldsymbol{\eta}}_n]^T$ for any integer n , and the state $\mathcal{A}_\theta(k_x)$, input $\mathcal{B}_\theta(k_x)$, and output $\mathcal{C}_\theta(k_x)$ matrices are bi-infinite with operator-valued elements in y ; see appendix A for details. We note that the input matrix $\mathcal{B}_\theta(k_x)$ results from the conversion of equation (3.3) into the evolution form (3.6) and the output matrix $\mathcal{C}_\theta(k_x)$ establishes a kinematic relation between the state $\boldsymbol{\psi}_\theta$ and the velocity vector \mathbf{v}_θ . At both the top and bottom walls of the channel, homogeneous Dirichlet and Neumann boundary conditions are imposed on \hat{v}_n , and homogeneous Dirichlet boundary conditions are imposed on $\hat{\boldsymbol{\eta}}_n$. Moreover, smoothness of the solution at the intersection

of the top and bottom wall-normal regions, i.e., $y = -1$, is ensured by enforcing the following conditions:

$$\begin{aligned}\hat{v}_n(y = -1^+, z) &= \hat{v}_n(y = -1^-, z), & \frac{\partial^i \hat{v}_n}{\partial y^i}(y = -1^+, z) &= \frac{\partial^i \hat{v}_n}{\partial y^i}(y = -1^-, z), \\ \hat{\eta}_n(y = -1^+, z) &= \hat{\eta}_n(y = -1^-, z), & \frac{\partial \hat{\eta}_n}{\partial y}(y = -1^+, z) &= \frac{\partial \hat{\eta}_n}{\partial y}(y = -1^-, z),\end{aligned}$$

with $i = \{1, 2, 3\}$.

3.3. Second-order statistics of the velocity fluctuations

The second-order statistics of the velocity fluctuations $\mathbf{v}_\theta(k_x, y, t)$ can be obtained from the solution $\mathcal{X}_\theta(k_x)$ of the operator Lyapunov equation (Fardad *et al.* 2008),

$$\mathcal{A}_\theta(k_x)\mathcal{X}_\theta(k_x) + \mathcal{X}_\theta(k_x)\mathcal{A}_\theta^*(k_x) = -\mathcal{M}_\theta(k_x). \quad (3.7)$$

Here, $*$ denotes the adjoint of an operator, $\mathcal{X}_\theta(k_x) := \langle \boldsymbol{\psi}_\theta(k_x, \cdot, t) \otimes \boldsymbol{\psi}_\theta(k_x, \cdot, t) \rangle$ is the steady-state covariance matrix of the state $\boldsymbol{\psi}_\theta(k_x, y, t)$, \otimes is the tensor product, and $\mathcal{M}_\theta(k_x) = \mathcal{M}_\theta^*(k_x) \succeq 0$ is the covariance matrix of the zero-mean white-in-time stochastic forcing $\mathbf{d}_\theta := \mathcal{B}_\theta \mathbf{f}_\theta$, i.e.,

$$\langle \mathbf{d}_\theta(k_x, \cdot, t_1) \otimes \mathbf{d}_\theta^*(k_x, \cdot, t_2) \rangle = \mathcal{M}_\theta(k_x) \delta(t_1 - t_2), \quad (3.8)$$

where δ is the Dirac delta function. Following the bi-infinite structure of $\mathbf{d}_\theta(k_x, \cdot, t)$, matrix $\mathcal{M}_\theta(k_x)$ takes the bi-infinite block-diagonal form $\mathcal{M}_\theta(k_x) = \text{diag} \{ \mathcal{M}(k_x, \theta_n) \}_{n \in \mathbb{Z}}$, where each block represents the covariance matrix of one of the harmonics of the forcing. Having obtained $\mathcal{X}_\theta(k_x)$, the covariance matrix of the velocity field $\mathbf{v}_\theta(k_x, \cdot, t)$ can be computed as $\Phi_\theta(k_x) = \mathcal{C}_\theta(k_x)\mathcal{X}_\theta(k_x)\mathcal{C}_\theta^*(k_x)$. Note that operator adjoints appearing in equation (3.7) for generator \mathcal{A}_θ or the expression of \mathcal{M}_θ (appendix C) should be determined with respect to the inner product that induces kinetic energy of flow fluctuations (Jovanovic & Bamieh 2005); see appendix A of Zare *et al.* (2017b) for a change of coordinates that provides a treatment by bringing equations (3.6) to a state-space in which the kinetic energy is determined by the Euclidean norm of the state vector.

Given its bi-infinite structure, solving Lyapunov equation (3.7) as done in Ran *et al.* (2021) and Naseri & Zare (2024) can become arduous, especially when considering sharp riblets (e.g., semi-circular riblets). This is because the long tails of the Fourier expansions (cf. equation(2.12)) give rise to a large number of significant harmonic interactions, and thereby, large dense matrices of dimension $2mN_y \times 2mN_y$ (for N_y collocation points in y and m harmonics in (2.12) and (2.13)) after discretization. We address this issue using a perturbation analysis of flow quantities in the height of riblets α , which allows us to break down equation (3.7), and thereby the analysis of all riblet-induced effects, over different perturbation levels. As we demonstrate, this technique, which exploits the structure of the block operator matrices in model (3.6), can provide sufficiently accurate solutions to equation (3.7) in a computationally efficient manner that facilitates analysis at high Reynolds numbers.

3.4. Perturbation analysis of flow statistics

In order to reduce the computational complexity of solving equation (3.7), we revisit § 2 and identify the height of riblets α determined by shape function (2.4) as a small parameter around which the mapping function $F(\tilde{y}, \tilde{z})$ can be expanded, i.e.,

$$F(\tilde{y}, \tilde{z}) = F_0(\tilde{y}) + \alpha F_1(\tilde{y}, \tilde{z}) + \alpha^2 F_2(\tilde{y}, \tilde{z}) + O(\alpha^3). \quad (3.9)$$

Here, $F_0(\tilde{y}) = \tilde{y}$, $F_1(\tilde{y}, \tilde{z}) = \bar{r}(\tilde{z})(\tilde{y} - 1)/2$, $F_2(\tilde{y}, \tilde{z}) = \bar{r}^2(\tilde{z})(\tilde{y} - 1)/4$ are obtained from the Neumann series expansion of $F(\tilde{y}, \tilde{z})$ given in equation (2.3) with $\bar{r}(\tilde{z}) = r(\tilde{z})/\alpha$. Following the structure of equation (2.11), a similar perturbation series can be considered for $U(y, z)$ as

$$U(y, z) = U_0(y) + \alpha U_1(y, z) + \alpha^2 U_2(y, z) + O(\alpha^3), \quad (3.10)$$

where $U_0(y)$, $U_1(y, z)$, and $U_2(y, z)$ can be consecutively obtained from the following sequence of linear equations:

$$\begin{aligned} \alpha^0 : \quad & \partial_y \left((1 + \nu_T) \partial_y U_0 \right) = \text{Re}_\tau \bar{P}_x \\ \alpha^1 : \quad & (1 + \nu_T) [\partial_{yy} + \partial_{zz}] U_1 + \nu'_T \partial_y U_1 = -2F_{\tilde{y}1} \partial_y \left((1 + \nu_T) \partial_y U_0 \right) \\ \alpha^2 : \quad & (1 + \nu_T) [\partial_{yy} + \partial_{zz}] U_2 + \nu'_T \partial_y U_2 = -(1 + \nu_T) [F_{\tilde{z}1}^2 \partial_{yy} U_0 + 2F_{\tilde{z}1} \partial_{yz} U_1] \\ & \quad - 2F_{\tilde{y}1} \partial_y \left((1 + \nu_T) \partial_y U_1 \right) - F_{\tilde{y}1}^2 \partial_y \left((1 + \nu_T) \partial_y U_0 \right). \end{aligned}$$

Note that $U_0(y)$ is the mean velocity profile for turbulent channel flow with smooth walls and $U_1(y, z)$ and $U_2(y, z)$ capture riblet-induced perturbations at the levels of α^1 and α^2 , respectively. Following the perturbation expansion for $F(\tilde{y}, \tilde{z})$ and $U(y, z)$ (equations (3.9) and (3.10)) in the linearized dynamics, the dynamic generator $\mathcal{A}_\theta(k_x)$ can be decomposed over various levels of α as

$$\mathcal{A}_\theta(k_x) = \mathcal{A}_{0,\theta}(k_x) + \alpha \mathcal{A}_{1,\theta}(k_x) + \alpha^2 \mathcal{A}_{2,\theta}(k_x) + O(\alpha^3), \quad (3.11)$$

where $\mathcal{A}_{0,\theta}(k_x)$ corresponds to turbulent channel flow over smooth walls and $\mathcal{A}_{1,\theta}(k_x)$ and $\mathcal{A}_{2,\theta}(k_x)$ captures the effect of riblets on the flow dynamics at α^1 and α^2 levels, respectively; see appendix B for the structure of block operator matrices $\mathcal{A}_{l,\theta}(k_x)$. As equation (3.7) is linear, its solution, $\mathcal{X}_\theta(k_x)$, inherits a similar perturbation series, i.e.,

$$\mathcal{X}_\theta(k_x) = \mathcal{X}_{0,\theta}(k_x) + \alpha \mathcal{X}_{1,\theta}(k_x) + \alpha^2 \mathcal{X}_{2,\theta}(k_x) + O(\alpha^3). \quad (3.12)$$

In appendix C, we show that $\mathcal{X}_{l,\theta}(k_x)$ are computed consecutively from smaller Lyapunov equations than (3.7) ($2N_y \times 2N_y$ vs $2mN_y \times 2mN_y$, for N_y collocation points in y and m harmonics in (2.12) and (2.13)). This highlights the computational advantage of our perturbation analysis over the analysis conducted in Ran *et al.* (2021). It is also noteworthy that the appearance of odd-powered perturbation terms in (3.11) and (3.12) is due to the offset introduced to $r(\tilde{z})$ in the mapping function $F(\tilde{y}, \tilde{z})$, which gives rise to 0th-order harmonics in (2.12). Finally, the energy spectrum of the flow can be computed as $\bar{E}_\theta(k_x) = \sum_{n \in \mathbb{Z}} \text{trace}(X_d(k_x, \theta_n))$, where $X_d(k_x, \theta_n)$ are blocks on the main diagonal of $\mathcal{X}_\theta(k_x)$ that have been confined to $y \in [-1, 1]$. Based on this, the perturbation series for $\mathcal{X}_\theta(k_x)$ yields the perturbation expansion

$$\bar{E}_\theta(k_x) = \bar{E}_{0,\theta}(k_x) + \alpha \bar{E}_{1,\theta}(k_x) + \alpha^2 \bar{E}_{2,\theta}(k_x) + O(\alpha^3) \quad (3.13)$$

for the energy spectrum of velocity fluctuations, where the energy at the level of α^l is computed from the trace of the corresponding covariance matrix in (3.12).

3.5. Perturbation analysis of turbulent viscosity

Based on the model adopted in § 3.1, the turbulent viscosity is determined by second-order statistics of the flow (cf. equations (3.2)), which can be computed from $X_d(k_x, \theta_n)$. Following (3.12), the perturbation analysis can be extended to the turbulent kinetic

energy k and its rate of dissipation ϵ as

$$\begin{aligned} k(y) &= k_0(y) + \alpha k_1(y) + \alpha^2 k_2(y) + O(\alpha^3), \\ \epsilon(y) &= \epsilon_0(y) + \alpha \epsilon_1(y) + \alpha^2 \epsilon_2(y) + O(\alpha^3), \end{aligned} \quad (3.14)$$

where the subscript 0 denotes quantities in the absence of riblets and subscripts 1 and 2 denote changes due to the effect of riblets, which can be computed from the corresponding terms in the perturbation series of $\mathcal{X}_\theta(k_x)$; see appendix D for details. Substituting (3.14) into (3.1) and employing the Neumann series expansion yields

$$\nu_T(y) = \nu_{T_0}(y) + \alpha \nu_{T_1}(y) + \alpha^2 \nu_{T_2}(y) + O(\alpha^3), \quad (3.15)$$

where ν_{T_0} is the turbulent viscosity for flows over smooth walls (equation (2.15)) and

$$\begin{aligned} \nu_{T_1}(y) &= \nu_{T_0}(y) \left(2 \frac{k_1(y)}{k_0(y)} - \frac{\epsilon_1(y)}{\epsilon_0(y)} \right), \\ \nu_{T_2}(y) &= \nu_{T_0}(y) \left(2 \frac{k_2(y)}{k_0(y)} - \frac{\epsilon_2(y)}{\epsilon_0(y)} - 2 \frac{\epsilon_1(y)k_1(y)}{\epsilon_0(y)k_0(y)} + \frac{\epsilon_1(y)^2}{\epsilon_0(y)^2} + \frac{k_1(y)^2}{k_0(y)^2} \right). \end{aligned} \quad (3.16)$$

Here, $k_0(y)$ captures the wall-normal dependence of turbulent kinetic energy in channel flow over smooth walls and can be computed from DNS-generated datasets (see, e.g., <https://torroja.dmt.upm.es/channels/data>). On the other hand, $\epsilon_0(y)$ is computed using $\epsilon_0(y) = cRe_\tau^2 k_0^2(y) / \nu_{T_0}(y)$. The influence of fluctuations on the turbulent mean velocity and, consequently, skin-friction drag can be quantified by substituting the perturbation series for F , U , and ν_T (equations (3.9), (3.10), and (3.15), respectively) into equation (2.11); see appendix E.

4. Turbulent drag reduction and kinetic energy suppression

We utilize the perturbation analysis presented in the previous section to study the effects of semi-circular riblets (figure 1(b)) with different geometric configurations (table 1) on the statistical signature of turbulent channel flow with $Re_\tau = 186$. In addition to analyzing changes to the energy spectrum, we use riblet-induced perturbations to the second-order statistics to compute changes to the mean velocity and skin-friction-drag. While the small size of riblets ($\alpha \ll 1$) enables our perturbation analysis, it also implies that the Reynolds number remains unchanged over various case studies as the influence of riblets on the channel height and shear velocity is negligible. We use 25 harmonics in z to capture the spanwise-periodic shape of the riblets via the domain transformation technique, i.e., $m \in [-12, 12]$ in the Fourier expansion (2.12). We use a DNS-generated dataset of flow statistics in channel flow over smooth walls (Del Álamo & Jiménez 2003; Del Álamo *et al.* 2004; Hoyas & Jiménez 2006) to compute $k_0(y)$ and $\epsilon_0(y)$ in equations (3.16) and to shape the energy spectrum of stochastic forcing $\mathbf{d}_\theta(k_x)$ in equation (3.8) (appendix C). In obtaining a finite-dimensional approximation of the evolution model (3.6), we use a total of N_y Chebyshev collocation points made up of N_t and N_b points in the top and bottom regions (i.e., $N_y = N_b + N_t$) to discretize the differential operators in the wall-normal direction. We also use N_x logarithmically spaced streamwise wavenumbers with $0.03 < k_x < k_{x,max}$ together with 3 harmonics of ω_z ($n = 1, 2$, and 3) and N_θ logarithmically spaced offset points $0.01 < \theta < \omega_z$ to parameterize the governing equations over the horizontal dimensions; see table (1). We ensure grid convergence by doubling the number of collocation points used for discretization in the wall-normal dimension and the number of wavenumbers used for

Re_τ	α/s	ω_z	N_x	N_t	N_b	N_θ	$k_{x,max}$
186	0.55	35, 40, 45, 60, 80, 100, 160	50	140	30	51	42.5
	0.65	45, 50, 60, 80, 100, 160					
	0.87	45, 50, 55, 60, 80, 100, 140, 160					
	1.2	60, 80, 100, 120, 160, 210					
547	0.55	115, 130, 175, 230, 290, 460	96	170	30	101	128
	0.65, 0.87, 1.2	115					
934	0.55	200, 220, 300, 390, 490, 780	192	200	30	151	255
	0.65, 0.87, 1.2	200					
2003	0.55	420, 470, 640, 840, 1050, 1700	384	270	10	201	511
	0.65, 0.87, 1.2	420					

TABLE 1. Characteristic parameters corresponding to various semi-circular riblet configurations examined in this study along with the number of discretization points used in different dimensions. Here, α/s and ω_z are the height-to-spacing ratio and spanwise frequency of riblets, N_t is the number of collocation points in the top wall-normal region (between -1 and $+1$), N_b is the number of collocation points in the bottom wall-normal region (between $-1 - \alpha r_p$ and -1), N_x is the number of wavenumbers in the streamwise direction, and N_θ is the number of logarithmically spaced offset wavenumbers $\theta < \omega_z$.

parameterization in the wall-parallel dimensions. While this section is dedicated to the validation of our approach at $Re_\tau = 186$, we exploit its true computational efficiency in exploring the physics of high-Reynolds-number channel flow over riblets in § 5.

4.1. Turbulent viscosity and turbulent mean velocity

We first examine the effect of semi-circular riblets with $\alpha/s = 0.87$ but different size on the turbulent viscosity and mean velocity. Figures 4(a) and 4(b) show the turbulent viscosity $\nu_{T_0}(y)$ and the mean velocity $U_0(y)$ profiles in channel flow with smooth walls, respectively. The wall-normal coordinate is in viscous units, i.e., $y^+ = Re_\tau(1 + y)$. Perturbation analysis allows us to separate the effect of riblets at α^1 and α^2 levels. As the spanwise variations (frequency) of riblet-induced perturbations to the turbulent viscosity and mean velocity are smaller than that of the surface roughness, all results are averaged over the spanwise dimension. While $\alpha \nu_{T_1}(y)$ shows a peak value located at $y^+ \approx 21$ for various sizes of riblets (figure 4(c)), $\alpha^2 \nu_{T_2}(y)$ shows a significant trough at $y^+ \approx 41$ (figure 4(e)). Given the typical values of α for which our perturbation analysis holds (e.g., $\alpha = 0.05$), an overall suppression of turbulence is observed after summing the effect at α and α^2 levels (cf. equation (3.15) and figure 4(g)), especially in the near-wall region. As shown in § 4.3, the near-wall suppression of ν_T results in an overall reduction in turbulent kinetic energy. We note, however, that roughness-induced turbulence suppression reduces for larger riblets. In a similar manner, figures 4(d) and 4(f) show the first- and second-order modifications to the mean velocity due to the presence of riblets. These corrective terms are obtained by substituting ν_{T_1} and ν_{T_2} into the mean flow equations (appendix E). In the vicinity of the wall, the dominant second-order term ($\alpha^2 \nu_{T_2}$) decreases the mean velocity resulting in a reduction in the mean velocity gradient relative to the baseline (figure 4(b)). At higher wall-normal locations, both αU_1 and $\alpha^2 U_2$ show an increase in the mean velocity gradient (figures 4(d) and 4(f)). In spite of this, the effect of small riblets ($\alpha \ll 1$) on the mean velocity is concentrated in the vicinity of lower wall (figure 4(h)).

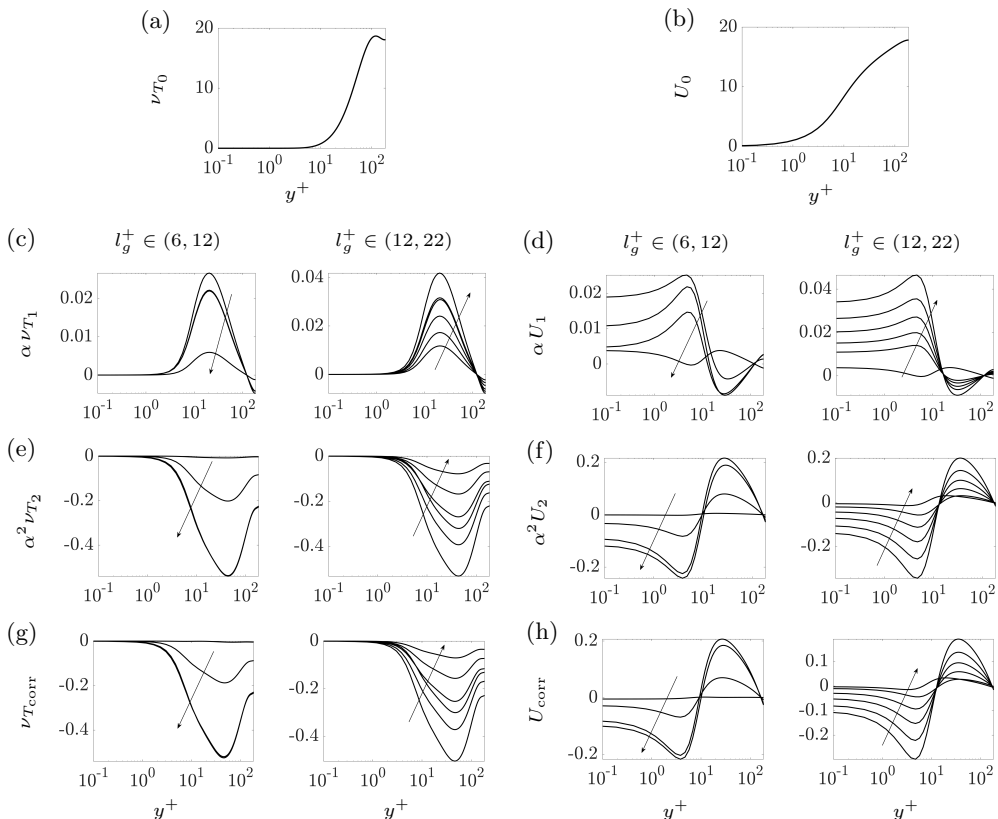


FIGURE 4. (a) Turbulent viscosity $\nu_{T_0}(y)$ and (b) mean velocity $U_0(y)$ in smooth channel flow with $Re_\tau = 186$ along with first- (c,d) and second-order (e,f) modifications to these quantities due to semi-circular riblets with $\alpha/s = 0.87$. The first and second columns in these subfigures correspond to small to optimal ($l_g^+ \in (6, 12)$) and optimal to large ($l_g^+ \in (12, 22)$) sized riblets, respectively. The final row shows the total modification (up to α^2) to (g) turbulent viscosity, i.e., $\nu_{T_{\text{corr}}} := \alpha \nu_{T_1} + \alpha^2 \nu_{T_2}$, and (h) the mean velocity, i.e., $U_{\text{corr}} := \alpha U_1 + \alpha^2 U_2$. In all figures, l_g^+ increases in the direction of the arrows.

In order to provide a point of comparison with the result of numerical simulations, figure 5(a) shows the mean velocity over semi-circular riblets with $\alpha/s = 0.87$ and $l_g^+ \approx 16$, which corresponds to the configuration considered in Choi *et al.* (1993) with a spanwise frequency of $\omega_z = 60$. While the mean velocity profiles from the DNS and our study show a good match for $y^+ \gtrsim 30$, they slightly deviate closer to the wall. This is because we have set the location of riblets to be slightly lower than those in the DNS to satisfy the constant bulk assumption. The spanwise variation of the mean velocity is depicted in figure 5(b). While the first-order modification $\alpha U_1(y, z)$ shows a concentration of riblet-induced effects in the vicinity of the wall ($y < -0.9$), the second-order modification $\alpha^2 U_2(y, z)$ shows high and low speed attributes alternating within the grooves and tips of the riblets that extend farther away from the wall.

4.2. Skin-friction drag

We next examine the effect of riblets on turbulent drag in flow with $Re_\tau = 186$. Following García-Mayoral & Jiménez (2011b), we refer to the parameter space in which drag reduction is proportional to the size of riblets as the viscous regime. Due to

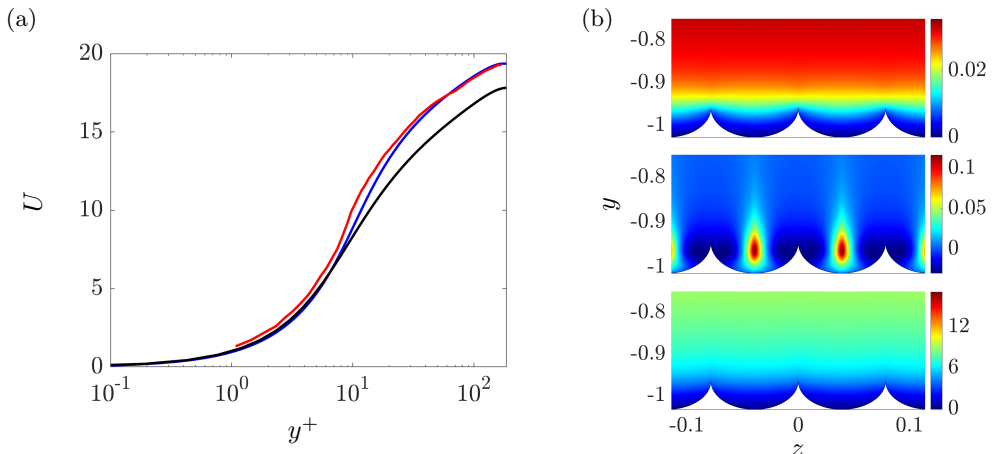


FIGURE 5. Mean velocity profiles of turbulent channel flow with $Re_\tau = 186$ over riblets with $\alpha/s = 0.87$ and $l_g^+ \approx 16$ ($\omega_z = 60$). (a) Spanwise-averaged profiles from our model (blue) and the DNS of Choi *et al.* (1993) (red) compared to the mean velocity in the absence of riblets (black); (b) Color plots of the y - z dependence of the riblet-induced modifications $\alpha U_1(y, z)$ (top), $\alpha^2 U_2(y, z)$ (middle) in addition to the resulting mean velocity $U(y, z)$ (bottom).

inconsistencies in analyzing the height and spacing of riblets of different shape, we use the square root of the cross-sectional area of the riblet grooves, $l_g^+ = \sqrt{A_g^+}$, for our parametric study. This geometric parameterization of riblets also achieves the best collapse of the breakdown dimensions for the linear viscous regime (García-Mayoral & Jiménez 2011*a, b*). We normalize the drag reduction curves by their slope in the viscous regime, i.e., $m_l := \lim_{l_g^+ \rightarrow 0} \Delta D/l_g^+$, to remove the effect of riblets' shape on the slope in this linear regime.

Figure 6 shows the m_l -normalized drag reduction as a function of l_g^+ for turbulent channel flow over semi-circular riblets with height-to-spacing ratios, $\alpha/s = \{0.55, 0.65, 0.87, 1.2\}$. For semi-circular riblets, the groove cross-section area is given by $A_g^+ = \pi/4 s^+ \alpha^+$, where the height and spacing are in inner viscous units, i.e., $\alpha^+ = Re_\tau \alpha$ and $s^+ = Re_\tau s$. Our model-based predictions of the range of optimal riblet sizes ($l_g^+ \in [9.6, 12.1]$) are in close agreement with $l_g^+ \in [9.7, 11.7]$ reported in existing literature (e.g., García-Mayoral & Jiménez (2011*b*)), and fall within the envelope of the experimental and numerical results (Bechert *et al.* 1997; García-Mayoral & Jiménez 2011*b*). We identify $\alpha/s = 0.87$ and $l_g^+ = 12.07$ ($\omega_z = 80$) as the optimal configuration for drag-reducing semi-circular riblets. Finally, we note that similar to prior studies (García-Mayoral & Jiménez 2011*b*), we observe a perfect collapse of drag reduction curves in the linear viscous regime followed by a breakdown and scattering beyond the optimal size. Given that a second-order perturbation analysis effectively captures the drag reduction trends observed in previous experimental and numerical studies, we confine our analysis to corrections of this order throughout the remainder of the paper.

4.3. Energy spectrum

In this section, we examine the effect of semi-circular riblets on the turbulent kinetic energy. Figure 7 compares the premultiplied energy spectrum of smooth channel flow, $k_x \theta E_0(\kappa)$, obtained from the DNS of Del Álamo & Jiménez (2003), with riblet-induced modifications resulting from our study. Here, $\kappa = (k_x, \theta)$, where θ is spanwise wavenumber offset. Following the parameterization in the spanwise direction, i.e., $\theta_n = \theta + n\omega_z$, the

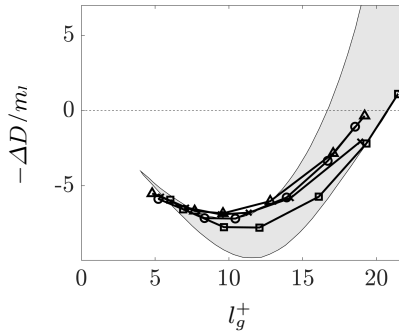


FIGURE 6. Normalized drag reduction due to semi-circular riblets on the lower wall of a turbulent channel flow with $Re_\tau = 186$ as a function of the square root of the riblet groove area l_g^+ . Different lines correspond to different riblet shapes: $\alpha/s = 0.55$ (Δ); $\alpha/s = 0.65$ (\circ); $\alpha/s = 0.87$ (\square); and $\alpha/s = 1.2$ (\times). The shaded region corresponds to the envelope of experimentally measured drag reduction levels from prior studies (Bechert *et al.* 1997; García-Mayoral & Jiménez 2011b).

energy spectra have been summed over n to integrate over the contributions of various harmonics. The figures show the premultiplied spectra so that the areas under the log-log plots are equal to the total energy of fluctuations.

Energy modulations at the α^1 and α^2 perturbation levels due to riblets with $\alpha/s = 0.87$ and $l_g^+ = 12.07$ are shown in figures 7(b) and 7(c), respectively. The most energetic modes of the smooth channel flow take place at $(k_x, \theta) \approx (2.2, 7.1)$ and the suppression of the turbulent kinetic energy due to the presence of the riblets is captured by darker colors in figure 7. The largest suppression happens at $(k_x, \theta) \approx (6.7, 12.1)$ and $(k_x, \theta) \approx (1.05, 8.85)$ for α^1 and α^2 levels, respectively. While figure 7(b) shows a slight energy amplification at $(k_x, \theta) \approx (0.73, 8.85)$, the overall effect, which is dominated by the second-order modification, does not show any suppression (figure 7(d)). The total effect of roughness (over all length-scales) on the turbulent kinetic energy can be determined by $\alpha^l \int_\kappa \bar{E}_l(\kappa) d\kappa / \int_\kappa \bar{E}_0(\kappa) d\kappa$ for different perturbation levels. For riblets with $l_g^+ = 12.07$ this quantity is 0.13% and -4.62% at α^1 and α^2 levels, respectively, and -4.49% overall. This riblet configuration also yields the largest drag reduction (cf. figure 6), which is suggestive of the direct correlation between drag reduction and energy suppression demonstrated by Ran *et al.* (2021). We note that the results shown thus far are also suggestive of the predominant role of second-order perturbations (at the α^2 level) in capturing riblet-induced modulations. Focusing on this term, figure 8 shows the dependence of the energy modulation on the height to spacing ratio α/s for other optimal riblet sizes. The riblet configurations considered in this figure uniformly suppress the energy of the flow with a similar spectral distribution as shown in figure 7(c) that is most pronounced for riblets with $\alpha/s = 0.65$ and $l_g^+ = 10.44$ ($\omega_z = 80$).

To more thoroughly investigate the impact of riblet size on the kinetic energy, we study the variation of this quantity in the wall-normal direction after averaging in the translationally invariant streamwise direction; see appendix D for details. To compare the kinetic energy at the riblet tips with the kinetic energy in smooth channel flow, an appropriate baseline is established at the origin sensed by the near-wall turbulence (Endrikat *et al.* 2021). For optimal riblets, this origin is located $\alpha(1 - r_p)$ below their tips. For larger than optimal riblets, the same origin is not sensed by the near-wall turbulence and we follow Endrikat *et al.* (2021) in defining the distance between the riblet tips and the origin based on the ratio of the protrusion height to the riblet height for the optimal riblets. Figure 9 compares the turbulent kinetic energy in smooth channel flow

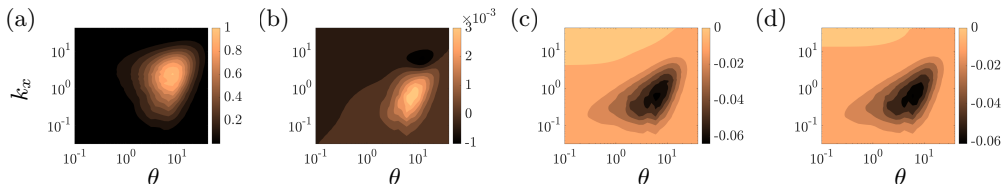


FIGURE 7. (a) Premultiplied energy spectrum of the smooth channel flow, $k_x \theta \bar{E}_0(\kappa)$ at $Re_\tau = 186$ from the DNS of Del Álamo & Jiménez (2003); (b) first-order ($\alpha k_x \theta \bar{E}_1(\kappa)$); (c) second-order ($\alpha^2 k_x k_z \bar{E}_2(\kappa)$); and (d) combined ($k_x \theta (\alpha \bar{E}_1(\kappa) + \alpha^2 \bar{E}_2(\kappa))$) modifications to the energy spectrum due to semi-circular riblets with height-to-spacing ratio $\alpha/s = 0.87$ and $l_g^+ = 12.07$ ($\omega_z = 80$).

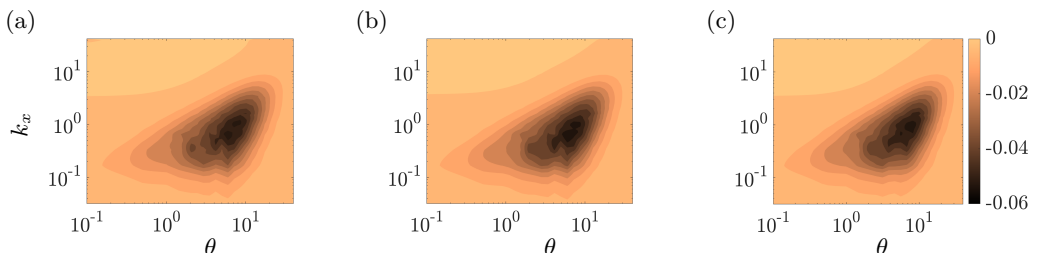


FIGURE 8. Second-order modifications to the premultiplied energy spectrum ($\alpha^2 k_x \theta \bar{E}_2(\kappa)$) of turbulent channel flow with $Re_\tau = 186$ due to lower-wall semi-circular riblets of optimal size with (a) $\alpha/s = 0.55$, $l_g^+ = 9.6$ ($\omega_z = 80$), (b) $\alpha/s = 0.65$, $l_g^+ = 10.44$ ($\omega_z = 80$), and (c) $\alpha/s = 1.2$, $l_g^+ = 9.45$ ($\omega_z = 120$).

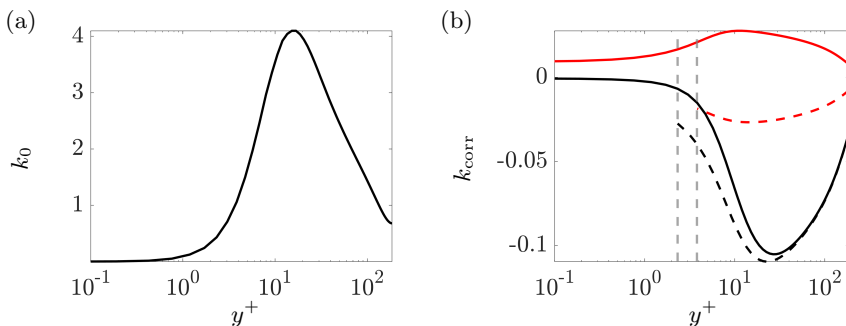


FIGURE 9. (a) Turbulent kinetic energy in smooth channel flow with $Re_\tau = 186$; (b) modifications $k_{\text{corr}} := \alpha k_1 + \alpha^2 k_2$, at the tip (dashed) and valley (solid) of semi-circular riblets with $\alpha/s = 0.87$ that reduce ($l_g^+ = 12.07$) and increase ($l_g^+ = 21.4$) drag are shown in black and red, respectively. The gray dashed lines mark the origins of profiles that start at the tips.

with $Re_\tau = 186$ with riblet-induced modifications to the turbulent kinetic energy above the tip and within the valley of semi-circular riblets with $\alpha/s = 0.87$ that either reduce ($l_g^+ = 12.07$) or increase ($l_g^+ = 21.4$) drag. In both cases, the kinetic energy is suppressed over the tips, with a more significant suppression observed for drag-reducing riblets. While the energy is also suppressed in the valley of drag-reducing riblets, it is amplified in the valley of drag-increasing riblets. This energy amplification is attributed to the downward penetration of streamwise vortices (Lee & Lee 2001).

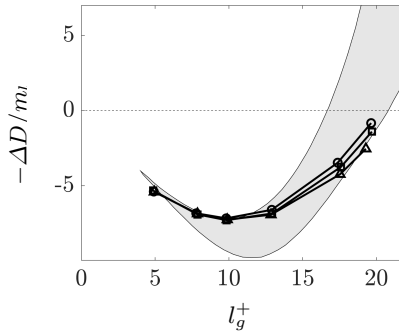


FIGURE 10. Drag reduction due to the presence of semi-circular riblets with $\alpha/s = 0.55$ for a turbulent channel flow with $Re_\tau = 547(\circ)$, $934(\square)$, and $2003(\triangle)$, as a function of the square root of the riblet groove area l_g^+ . The shaded region envelopes experimentally measured drag reduction levels from prior studies (Bechert *et al.* 1997; García-Mayoral & Jiménez 2011*b*).

5. Analysis of flow mechanisms in the presence of riblets

In this section, we leverage the computational efficiency of our framework to study the flow mechanisms that affect the drag reducing abilities of riblets at high Reynolds numbers. The riblet configurations considered in this part of our study are summarized in table (1). Figure 10 shows the m_l -normalized drag reduction for turbulent channel flow with $Re_\tau = 547$, 934 , and 2003 over semi-circular riblets with $\alpha/s = 0.55$. The degradation of drag reduction observed for large l_g^+ is due to non-negligible inertial-flow mechanisms that lead to the eventual breakdown of the linear viscous regime in the drag reduction curve (Modesti *et al.* 2021). Examples of such mechanisms that have been studied in the past include the lodging of near-wall vortices inside riblet grooves (Choi *et al.* 1993; Suzuki & Kasagi 1994; Lee & Lee 2001), the generation of secondary flow (Goldstein & Tuan 1998), and the emergence of spanwise coherent rollers (García-Mayoral & Jiménez 2011*b*). Herein, we examine the appearance and prevalence of spanwise rollers induced by the K-H instability and the re-organization of turbulence in the vicinity of riblet-mounted surfaces, which have been the topic of more recent numerical studies on large and sharp riblets (Endrikat *et al.* 2021, 2022).

In a similar manner to the proper orthogonal decomposition of Bakewell & Lumley (1967); Moin & Moser (1989), our analysis is facilitated by steady-state flow structures that can be constructed from the eigenvectors of the covariance matrix

$$\Phi_\theta(k_x) = \mathcal{C}_\theta(k_x)\mathcal{X}_\theta(k_x)\mathcal{C}_\theta^*(k_x), \quad (5.1)$$

where, $\mathcal{X}_\theta(k_x)$ is the solution to the Lyapunov equation (3.7). The eigenvectors associated with the principal pair of eigenvalues of this covariance matrix are typically representative of energetically dominant flow structures that reside in the vicinity of the upper and lower channel walls. Based on this and channel symmetries, the velocity components corresponding to such flow structures can be obtained as

$$\begin{aligned} u(x, y, z) &= \int_{k_x, \theta_n > 0} \text{Re}(\hat{u}(y, \kappa)e^{ik_x x}) \cos(\theta_n z) d\kappa, \\ v(x, y, z) &= \int_{k_x, \theta_n > 0} \text{Re}(\hat{v}(y, \kappa)e^{ik_x x}) \cos(\theta_n z) d\kappa, \\ w(x, y, z) &= -\int_{k_x, \theta_n > 0} \text{Im}(\hat{w}(y, \kappa)e^{ik_x x}) \sin(\theta_n z) d\kappa. \end{aligned} \quad (5.2)$$

where Re and Im denote the real and imaginary parts of the streamwise (\hat{u}), wall-normal (\hat{v}), and spanwise (\hat{w}) components of the dominant eigenvectors of $\Phi_\theta(k_x)$.

5.1. Kelvin-Helmholtz instability

The emergence of long spanwise rollers induced by the K-H instability marks the onset of the breakdown of the linear viscous regime, leading to a reduced effectiveness of riblets in drag reduction (García-Mayoral & Jiménez 2011*b*). This process enhances momentum exchange within and around the riblet grooves, leaving a distinct imprint on the wall-normal and shear stress energy spectra (García-Mayoral & Jiménez 2011*b*; de Segura & García-Mayoral 2019; Sharma & García-Mayoral 2020). In this subsection, we analyze the spectral footprint of K-H rollers using our modeling framework.

5.1.1. Effect of Kelvin-Helmholtz instability on the wall-normal energy spectrum

Figure 11 analyzes riblet-induced changes to the premultiplied wall-normal energy spectrum $k_x k_z E_{vv}$ of channel flow with $Re_\tau = 547$ over a horizontal plane located 1 viscous unit above the riblet crests. In this figure, streamwise and spanwise wavelengths are expressed in viscous units with $\lambda_x^+ = 2\pi Re_\tau / k_x$ and $\lambda_z^+ = 2\pi Re_\tau / \theta$. As riblet size increases, the wall-normal energy spectrum transitions from a damping trend to one that progressively amplifies, within a spectral range corresponding to the typical wavelengths of spanwise rollers, i.e., $65 < \lambda_x^+ < 290$ and $\lambda_z^+ > 130$. This trend, which is uniformly observed at both α^1 and α^2 levels of our perturbation analysis, is in agreement with the observations of prior numerical studies (García-Mayoral & Jiménez 2011*b*; Endrikat *et al.* 2021). Interestingly, we also observe that larger riblets suppress the energy of the wall-normal velocity at the most energetic wavelengths of smooth channel flow; see regions delimited by white solid lines in the middle and right columns of figure 11. To investigate how things would change for larger riblets, figure 12 extends the cases studied in figure 11 to $l_g^+ \approx 22, 25, \text{ and } 29$ ($\omega_z = 115$ for all three). The premultiplied modifications to the wall-normal energy spectra again show amplification for wavelengths delimited by the solid black lines. This amplification is larger for taller riblets. For all cases, energy amplification peaks at $\lambda_x^+ \approx 230$ and persists over the longest spanwise wavelengths ($\lambda_z^+ \gtrsim 100$) corresponding to the wide rollers excited by the K-H instability (García-Mayoral & Jiménez 2011*b*) especially over large and sharp riblets (Endrikat *et al.* 2021). Finally, we observe that the spectral modifications to the wall-normal energy spectra are consistent across the cases presented in figure 12, which is suggestive of a potential geometric scaling of this quantity for large (i.e., larger than optimal) riblets.

Figure 13 shows the effect of lower-wall semi-circular riblets with $\alpha/s = 0.55$ and $l_g^+ \approx 20$ on the wall-normal energy spectrum at different Reynolds numbers. The case of $Re_\tau = 547$ is repeated from figure 11(i) for ease of comparison. It is evident from this figure that the energy amplification in the spectral window associated with the K-H instability is strengthened for higher Reynolds numbers. This trend is suggestive of the more pronounced footprint of K-H rollers and their earlier appearance in riblets with smaller l_g^+ at higher Reynolds numbers. However, we note that the shift toward smaller riblets inducing the K-H instability becomes less pronounced at higher Reynolds numbers, which is in agreement with the results of García-Mayoral & Jiménez (2012).

For channel flow with $Re_\tau = 547$ over optimal to large-size semi-circular riblets with $\alpha/s = 0.55$, figure 14 shows the wall-normal profiles of the modifications to the wall-normal stress given by

$$vv_{\text{KH}}(y) = \int_{130}^{1000} \int_{65}^{290} (\alpha E_{vv,1} + \alpha^2 E_{vv,2}) d\lambda_x^+ d\lambda_z^+. \quad (5.3)$$

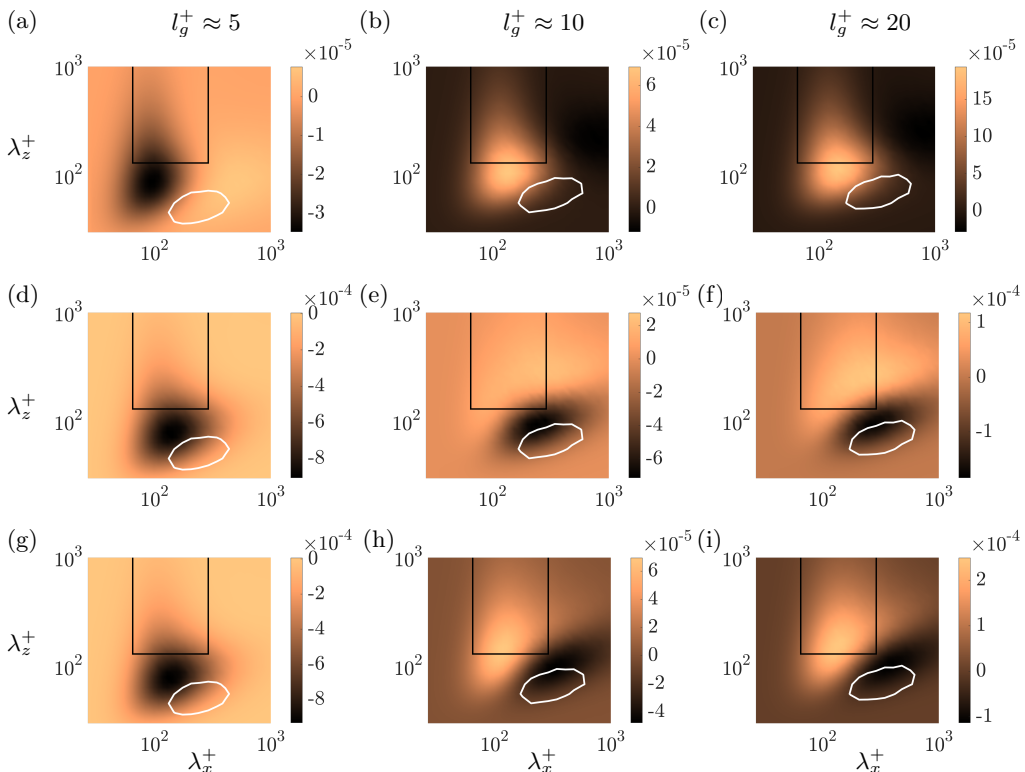


FIGURE 11. Premultiplied modifications to the wall-normal energy spectrum of turbulent channel flow with $Re_\tau = 547$ one viscous unit above the crest of semi-circular riblets with $\alpha/s = 0.55$ and $l_g^+ \approx 5$ ($\omega_z = 460$) (left column), $l_g^+ \approx 10$ ($\omega_z = 230$) (middle column), and $l_g^+ \approx 20$ ($\omega_z = 115$) (right column). (a-c) $\alpha k_x k_z E_{vv,1}$; (d-f) $\alpha^2 k_x k_z E_{vv,2}$; and (g-i) $k_x k_z (\alpha E_{vv,1} + \alpha^2 E_{vv,2})$. Black lines delimit the spectral window of K-H rollers according to García-Mayoral & Jiménez (2011b) and white solid lines correspond to the 80% contour level of the energy spectrum of smooth channel flow from the DNS of Del Álamo *et al.* (2004).

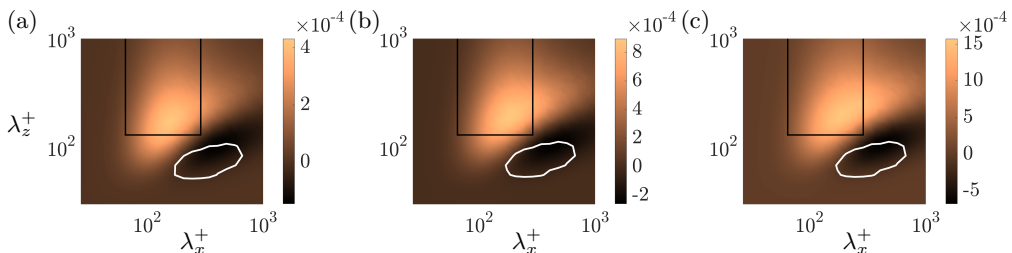


FIGURE 12. Premultiplied modifications to the wall-normal energy spectrum, $k_x k_z (\alpha E_{vv,1} + \alpha^2 E_{vv,2})$, of turbulent channel flow with $Re_\tau = 547$ one viscous unit above the crest of semi-circular riblets with the same viscous spacing but different viscous height. (a) $\alpha/s = 0.65$ and $l_g^+ \approx 22$ ($\omega_z = 115$); (b) $\alpha/s = 0.87$ and $l_g^+ \approx 25$ ($\omega_z = 115$); and (c) $\alpha/s = 1.2$ and $l_g^+ \approx 29$ ($\omega_z = 115$). Black lines delimit the spectral window of K-H rollers (García-Mayoral & Jiménez 2011b) and white solid lines correspond to the 80% contour level of the energy spectrum of smooth channel flow from the DNS of Del Álamo *et al.* (2004).

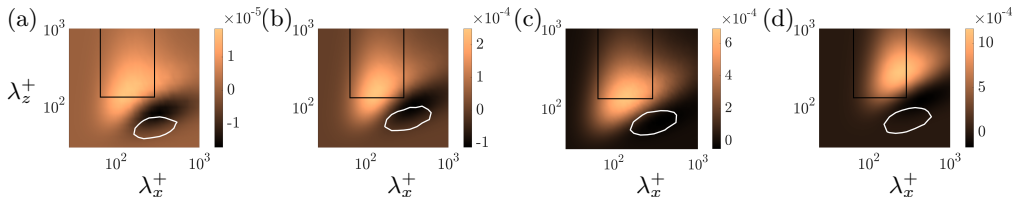


FIGURE 13. Premultiplied modifications to the wall-normal energy spectrum $k_x k_z (\alpha E_{vv,1} + \alpha^2 E_{vv,2})$ for turbulent channel flow with (a) $Re_\tau = 186$, (b) $Re_\tau = 547$, (c) $Re_\tau = 934$, and (d) $Re_\tau = 2003$ one viscous unit above the crest of semi-circular riblets with $\alpha/s = 0.55$ and $l_g^+ \approx 20$, which corresponds to spatial frequencies $\omega_z = 40, 115, 200$, and 420 , respectively. Black lines delimit the spectral window of K-H rollers and white solid lines correspond to the 80% contour level in the energy spectrum of smooth channel flow from the DNS of Del Álamo & Jiménez (2003); Del Álamo *et al.* (2004); Hoyas & Jiménez (2006).

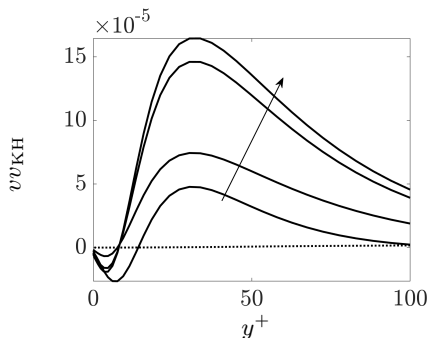


FIGURE 14. Modifications to the wall-normal stress vv_{KH} resulting from the K-H modes in channel flow with $Re_\tau = 547$ over semi-circular riblets with $\alpha/s = 0.55$ and $l_g^+ \in (10, 20)$ ($\omega_z \in [115, 230]$). The black dotted line corresponds to the profile computed using (5.3) in the absence of riblets and l_g^+ increases in the direction of the arrow.

Integration over $65 < \lambda_x^+ < 290$ and $130 < \lambda_z^+ < 1000$ ensures a separation of scales from the near-wall cycle at larger λ_x^+ and the association with the K-H instability and is achieved by integrating over the k_x and θ_n values associated with the targeted wavelengths. Modifications to the wall-normal stress profile peak at $y^+ \approx 36$. Moreover, we observe the peak values to increase for larger riblets. The emergence of these peaks, driven by the K-H instability, indicates elevated turbulence levels on riblet-mounted surfaces compared to smooth walls, and is in agreement with the findings of García-Mayoral & Jiménez (2011b).

5.1.2. Effect of Kelvin-Helmholtz instability on the shear stress

In addition to its imprint on the wall-normal energy spectrum, the K-H instability also results in an increase in the Reynolds shear stress, which, consequently, affects momentum transfer and skin-friction drag (García-Mayoral & Jiménez 2011b; de Segura & García-Mayoral 2019). Figure 15 shows the riblet-induced changes to the premultiplied energy spectrum of Reynolds shear stress $k_x k_z E_{uv}$ of channel flow with $Re_\tau = 547$ over a horizontal plane located 1 viscous unit above the riblet crests. As the riblet size increases, the energy spectra show more amplification at both α^1 and α^2 levels. These observations are similar to that of the wall-normal energy spectrum (figure 11). To investigate the effect of larger riblets, figure 16 includes the cases with $l_g^+ \approx 22, 25$, and 29 ($\omega_z = 115$ for all three). The premultiplied energy spectrum of the Reynolds shear stress is again amplified, and it gets stronger for taller riblets. The similarity of the energy modification

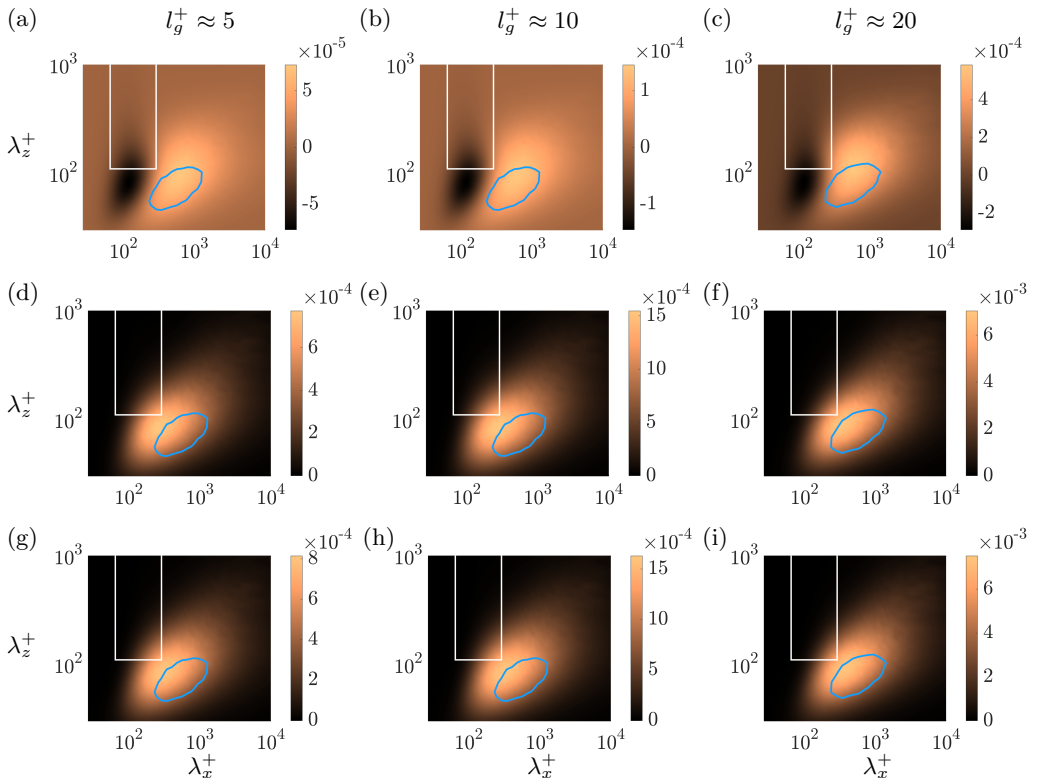


FIGURE 15. Premultiplied modifications to the energy spectrum of Reynolds shear stress in channel flow with $Re_\tau = 547$ one viscous unit above the crest of semi-circular riblets with $\alpha/s = 0.55$ and $l_g^+ \approx 5$ ($\omega_z = 460$) (left column), $l_g^+ \approx 10$ ($\omega_z = 230$) (middle column), and $l_g^+ \approx 20$ ($\omega_z = 115$) (right column). (a-c) $\alpha k_x k_z E_{uv,1}$; (d-f) $\alpha^2 k_x k_z E_{uv,2}$; and (g-i) $k_x k_z (\alpha E_{uv,1} + \alpha^2 E_{uv,2})$. White solid lines delimit the spectral window of K-H rollers according to García-Mayoral & Jiménez (2011b) and blue solid lines correspond to the 70% contour level of the energy spectrum of smooth channel flow from the DNS of Del Álamo *et al.* (2004).

patterns for riblets with the same spanwise frequency ω_z and different sizes suggests a potential geometric scaling of this quantity. Finally, figure 17 compares the influence of riblets with $\alpha/s = 0.55$ and $l_g^+ \approx 20$ on the energy spectrum of the Reynolds shear stress over different Reynolds numbers. The case of $Re_\tau = 547$ is repeated from figure 15(i) for ease of comparison. It is apparent that energy amplification in the spectral window associated with the K-H instability is strengthened at higher Reynolds numbers, similar to that of the wall-normal energy spectrum (figure 13).

For channel flow with $Re_\tau = 547$ over optimal to large-size semi-circular riblets with $\alpha/s = 0.55$, figure 18 shows the wall-normal profiles of the modifications to the streamwise-wall-normal stress profile given by

$$uv_{\text{KH}}(y) = \int_{130}^{1000} \int_{65}^{290} (\alpha E_{uv,1} + \alpha^2 E_{uv,2}) d\lambda_x^+ d\lambda_z^+. \quad (5.4)$$

Modifications to the shear stress peak at $y^+ \approx 3$, and the peak values increase for larger riblets. The emergence of these peaks indicates that the structures with those wavelengths carry a significant part of the energy in the flow (García-Mayoral & Jiménez 2012; Endrikat *et al.* 2021).

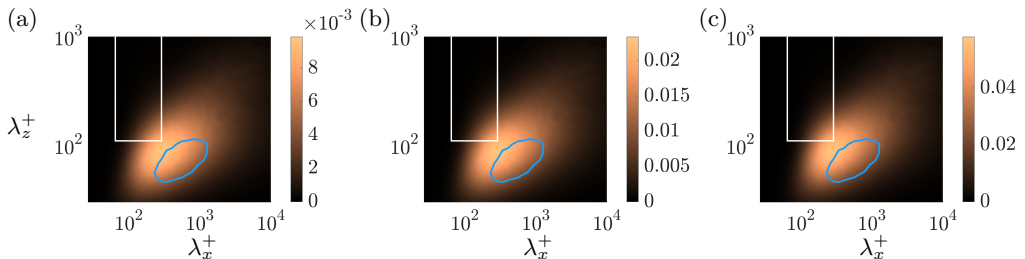


FIGURE 16. Premultiplied modifications to the energy spectrum of Reynolds shear stress, $k_x k_z (\alpha E_{uv,1} + \alpha^2 E_{uv,2})$, of turbulent channel flow with $Re_\tau = 547$ one viscous unit above the crest of semi-circular riblets with the same viscous spacing but different viscous height. (a) $\alpha/s = 0.65$ and $l_g^+ \approx 22$ ($\omega_z = 115$); (b) $\alpha/s = 0.87$ and $l_g^+ \approx 25$ ($\omega_z = 115$); and (c) $\alpha/s = 1.2$ and $l_g^+ \approx 29$ ($\omega_z = 115$). White lines delimit the spectral window of K-H rollers according to García-Mayoral & Jiménez (2011b) and blue solid lines correspond to the 70% contour level of the energy spectrum of smooth channel flow from the DNS of Del Álamo *et al.* (2004).

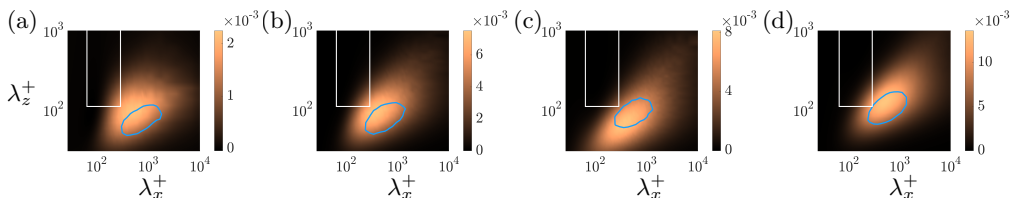


FIGURE 17. Riblet-induced modifications to the energy spectrum of Reynolds shear stress $k_x k_z (\alpha E_{uv,1} + \alpha^2 E_{uv,2})$ for turbulent channel flow with (a) $Re_\tau = 186$, (b) $Re_\tau = 547$, (c) $Re_\tau = 934$, and (d) $Re_\tau = 2003$ one viscous unit above the crest of semi-circular riblets with $\alpha/s = 0.55$ and $l_g^+ \approx 20$, which corresponds to spatial frequencies $\omega_z = 40, 115, 200$, and 420, respectively. White lines delimit the spectral window of K-H rollers and blue solid lines correspond to the 70% contour level in the energy spectrum of smooth channel flow from the DNS of Del Álamo & Jiménez (2003); Del Álamo *et al.* (2004); Hoyas & Jiménez (2006).

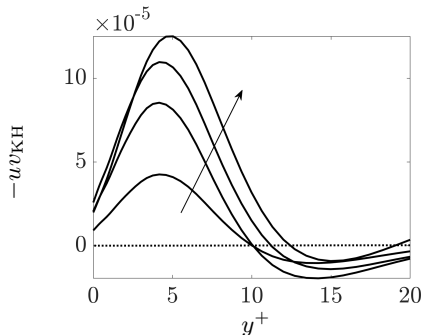


FIGURE 18. Modifications to the shear stress $-uv_{KH}$ resulting from the K-H modes in channel flow with $Re_\tau = 547$ over semi-circular riblets with $\alpha/s = 0.55$ and $l_g^+ \in (10, 20)$ ($\omega_z \in [115, 230]$). The black dotted line corresponds to the profile computed using (5.4) in the absence of riblets and l_g^+ increases in the direction of the arrow.

Figure 19 compares the one-dimensional energy spectrum of Reynolds shear stress $-k_x E_{uv}$ in smooth turbulent channel flow with $Re_\tau = 547$ with modifications $-k_x (\alpha E_{uv,1} + \alpha^2 E_{uv,2})$ due to different lower-wall riblet configurations. We observe that the shear stress spectrum is strengthened in the near-wall region ($y^+ < 10$) and that the amplification becomes stronger for larger riblets. This near-wall amplification

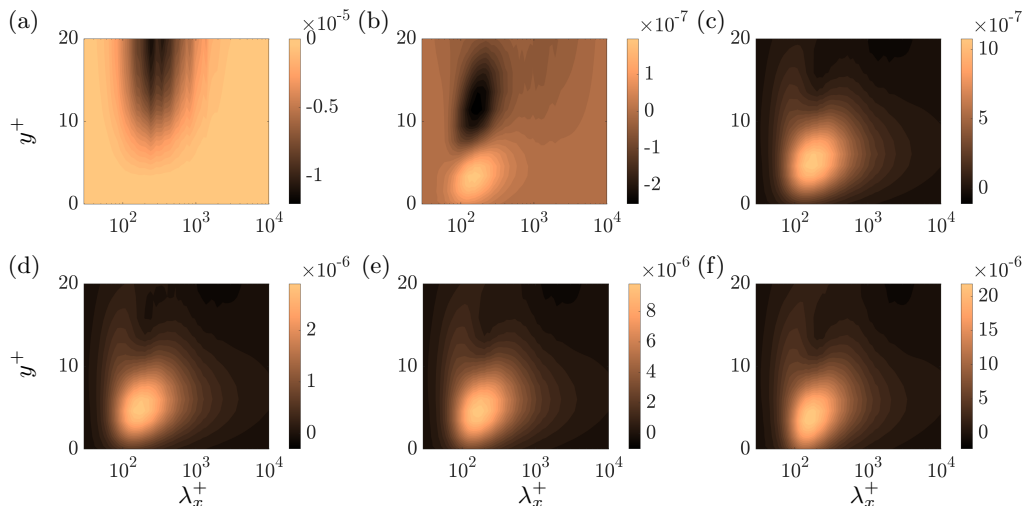


FIGURE 19. (a) Premultiplied one-dimensional energy spectrum of Reynolds shear stress, $-k_x E_{uv}$, integrated over spanwise wavelengths $\lambda_z^+ > 130$ for smooth channel flow from the DNS of Del Álamo *et al.* (2004). (b, c) Premultiplied modifications to the one-dimensional energy spectrum of Reynolds shear stress, $-k_x(\alpha E_{uv,1} + \alpha^2 E_{uv,2})$, integrated over $\lambda_z^+ > 130$ for channel flow with $Re_\tau = 547$ over semi-circular riblets with $\alpha/s = 0.55$ and $l_g^+ \approx 10$ ($\omega_z = 230$) (b) and $l_g^+ \approx 20$ ($\omega_z = 115$) (c). (d-f) The same quantity for large semi-circular riblets that share the same viscous spacing as the case in (c) but different height: (d) $\alpha/s = 0.65$ and $l_g^+ \approx 22$ ($\omega_z = 115$); (e) $\alpha/s = 0.87$ and $l_g^+ \approx 25$ ($\omega_z = 115$); and (f) $\alpha/s = 1.2$ and $l_g^+ \approx 29$ ($\omega_z = 115$).

corresponds to the excitation of large spanwise-coherent motions (Endrikat *et al.* 2021). Figures 19(c-f) show that for riblets with the same spacing, the Reynolds shear stress becomes stronger in the near-wall region. The peak value is concentrated at $y^+ \approx 5$ and $\lambda_x^+ \approx 180$, which specifies the dominant streamwise wavelength for K-H rollers. Moreover, larger riblets slightly increase the dominant streamwise wavelength. This observation is in agreement with previous studies on K-H rollers in flows over filament canopies (Sharma & García-Mayoral 2020) and riblets (Endrikat *et al.* 2021). We also observe an expanding presence of Reynolds shear stress within the riblet grooves as their size increases, aligning with the observed decline in their drag-reduction effectiveness (figure 10).

5.1.3. Effect of Kelvin-Helmholtz instability on the wall-normal velocity

Previous numerical studies reveal the presence of K-H rollers that arise from the amplification mechanisms described in prior figures using instantaneous visualizations of wall-normal velocity (García-Mayoral & Jiménez 2011b; García-Mayoral & Jiménez 2012). The excitation of such flow structures can also be captured by analyzing the dominant eigenmode of the covariance matrices $\Phi_\theta(k_x)$ for $65 < \lambda_x^+ < 290$ and $130 < \lambda_z^+ < 1000$. As shown in figure 20, the visualization of this eigenmode illustrates alternating patterns of downwash and upwash flow across several riblet grooves. The riblets considered in this figure are semi-circular with $\alpha/s = 0.55$ and $l_g^+ \approx 20$ for $Re_\tau = 186, 547, 934$, and 2003. Coherent regions of high and low wall-normal velocity are observed in all cases with spanwise vortices becoming larger. The intensity of high and low-speed regions also increases with the Reynolds number, which is attributed to the interaction of outer-layer structures with the spanwise rollers (García-Mayoral &

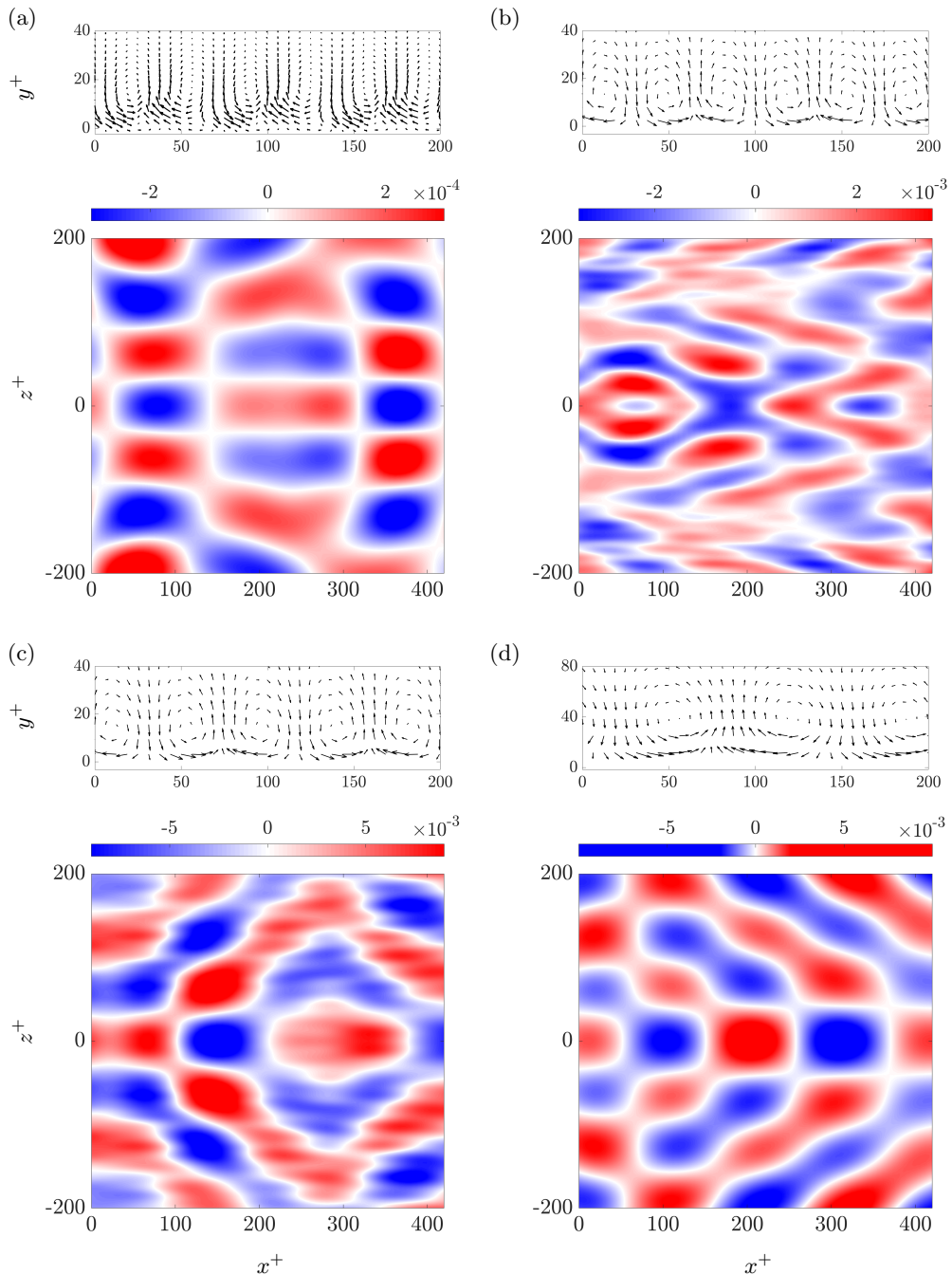


FIGURE 20. Velocity vectors (u, v) corresponding to spanwise vortices (top) and colorplots of the wall-normal velocity v (bottom) in channel flow with (a) $Re_\tau = 186$, (b) $Re_\tau = 547$, (c) $Re_\tau = 934$, and (d) $Re_\tau = 2003$ over riblets with $\alpha/s = 0.55$ and $l_g^+ \approx 20$, which corresponds to spatial frequencies $\omega_z = 40, 115, 200$, and 420 , respectively. Flow patterns result from a superposition of dominant eigenmodes of the covariance matrix $\Phi_\theta(k_x)$ for $65 < \lambda_x^+ < 290$ and $130 < \lambda_z^+ < 1000$. The wall-normal x - y planes correspond to $z^+ = 0$ and the wall-parallel x - z planes correspond to $y^+ \approx 5$, i.e., one viscous unit above the crest of riblets.

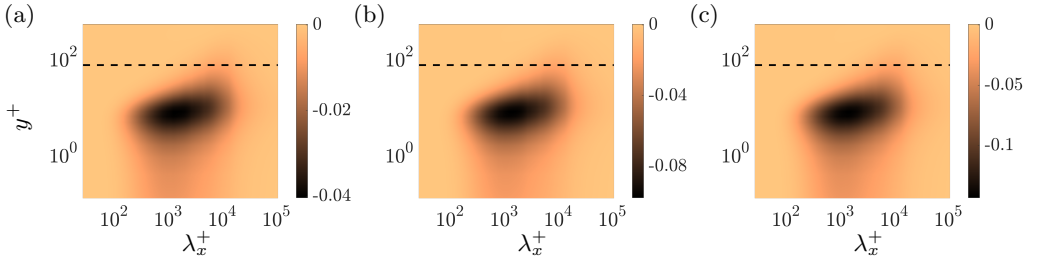


FIGURE 21. Premultiplied modifications to the one-dimensional energy spectrum of streamwise velocity, $k_x(\alpha E_{uu,1} + \alpha^2 E_{uu,2})$, integrated over all spanwise wavelengths in channel flow with $Re_\tau = 547$ over semi-circular riblets with $\alpha/s = 0.55$ and (a) $l_g^+ \approx 5$ ($\omega_z = 460$); (b) $l_g^+ \approx 10$ ($\omega_z = 230$); and (c) $l_g^+ \approx 20$ ($\omega_z = 115$). The black dashed lines correspond to the lower bound of the logarithmic layer.

Jiménez 2012) above the tips of large riblets. As a result, the wall-normal momentum transfer and turbulent mixing increases, which causes an increase in the drag. Finally, we observe a shift in the core of spanwise rollers from $y^+ \approx 10$ in flow with $Re_\tau = 186$ to $y^+ \approx 38$ in flow with $Re_\tau = 2003$ with an extension to the bottom wall.

5.2. Near-wall cycle

The near-wall regeneration cycle involves the formation of streaks driven by the advection of the mean profile by streamwise vortices, which themselves arise from streak instabilities (Hamilton *et al.* 1995; Jiménez & Pinelli 1999; Schoppa & Hussain 2002; Jiménez 2013; Hwang & Bengana 2016). The presence of large sharp riblets can affect the structure and energy of such energetic motions (Endrikat *et al.* 2022). In this section, we study the energy and spatial attributes of dominant motions that reside close to the corrugated surface of the channel. Figure 21 shows riblet-induced changes to the premultiplied one-dimensional streamwise energy spectrum $k_x E_{uu}$ integrated over all spanwise wavelengths in channel flow with $Re_\tau = 547$. As the riblet size becomes larger, the large streamwise wavelengths are suppressed in the near-wall region below the logarithmic layer (Endrikat *et al.* 2022). The similarity between the spectral modifications suggests a potential geometric scaling over all riblet sizes. To study the effect of the corrugation height, we further increase the riblet size but with a constant spacing in figure 22. The modifications to the one-dimensional streamwise energy spectra again expose the suppression of large wavelengths in the near-wall region but with a slightly higher reach in the case of taller riblets. In all cases, maximum attenuation happens for $\lambda_x^+ \approx 1300$ at $y^+ \approx 6$, which indicates the suppression of the near-wall portion of streamwise-elongated flow structures.

Figure 23 shows the effect of lower-wall semi-circular riblets with $\alpha/s = 0.55$ and $l_g^+ \approx 20$ on the one-dimensional streamwise energy spectrum of turbulent channel flow with different Reynolds numbers. The case of $Re_\tau = 547$ is repeated from figure 21(c) for ease of comparison. It is evident that the streamwise-elongated structures are more suppressed at higher Reynolds numbers. While the effect of riblets is largely concentrated to the buffer layer, their wall-normal reach can clearly protrude into the logarithmic layer at higher Reynolds numbers (figures 23(c) and 23(d)). These observations are in agreement with that of Endrikat *et al.* (2022), in which DNS of minimal channel flow was combined with experiments to study the effect of large riblets in high-Reynolds-number wall-bounded flows up to $Re_\tau = 1000$. The aforementioned study, however, identified the regions of missing energy at larger streamwise wavelengths ($\lambda_x^+ \approx 5000$).

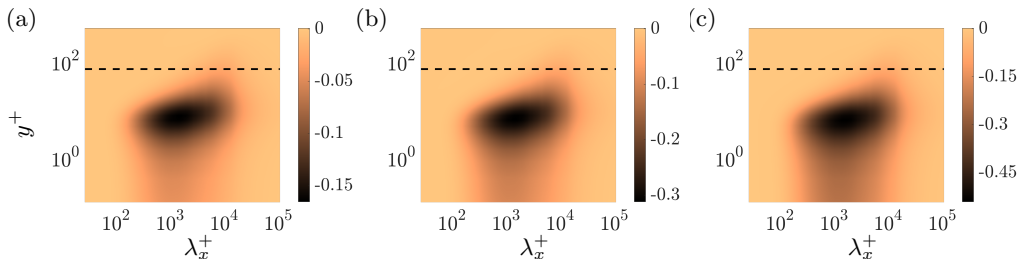


FIGURE 22. Premultiplied modifications to the one-dimensional energy spectrum of streamwise velocity, $k_x(\alpha E_{uu,1} + \alpha^2 E_{uu,2})$, integrated over all spanwise wavelengths in channel flow with $Re_\tau = 547$ over semi-circular riblets with the same viscous spacing but different viscous height. (a) $\alpha/s = 0.65$ and $l_g^+ \approx 22$ ($\omega_z = 115$); (b) $\alpha/s = 0.87$ and $l_g^+ \approx 25$ ($\omega_z = 115$); and (c) $\alpha/s = 1.2$ and $l_g^+ \approx 29$ ($\omega_z = 115$). The black dashed lines correspond to the lower bound of the logarithmic layer.

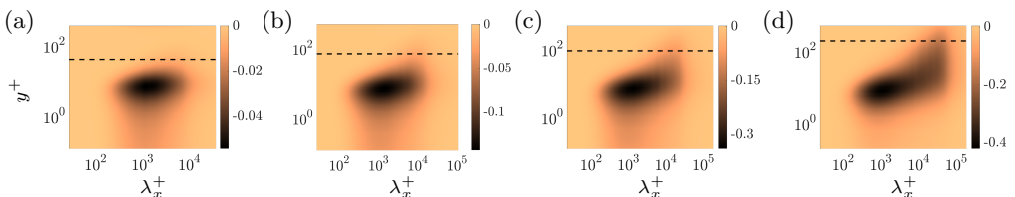


FIGURE 23. Premultiplied modifications to the one-dimensional energy spectrum of streamwise velocity, $k_x(\alpha E_{uu,1} + \alpha^2 E_{uu,2})$, integrated over all spanwise wavelengths in channel flow with (a) $Re_\tau = 186$, (b) $Re_\tau = 547$, (c) $Re_\tau = 934$, and (d) $Re_\tau = 2003$ over semi-circular riblets of $\alpha/s = 0.55$ and $l_g^+ \approx 20$, which corresponds to spatial frequencies $\omega_z = 40, 115, 200,$ and 420 , respectively. The black dashed lines correspond to the lower bound of the logarithmic layer.

Figure 24 compares the dominant near-wall flow structures for turbulent channel flow with $Re_\tau = 547$ over small ($l_g^+ \approx 5$), optimal ($l_g^+ \approx 10$), and large ($l_g^+ \approx 20$) semi-circular riblet configurations that share the height to spacing ratio of $\alpha/s = 0.55$. The wavelengths of these flow structures, i.e., $(\lambda_x^+, \lambda_z^+) \approx (1100, 110)$, correspond to the typical length scales that dominate the near-wall cycle (Jiménez & Pinelli 1999). The periodicity of the targeted flow structures in the horizontal plane is reflected in the planar views of figure 24 as regions of high and low streamwise velocity that encompass the surface corrugation on the lower wall. As evident from figure 24(b), small riblets have little to no effect on the near-wall structures, i.e., the flow structures resemble streamwise-elongated flow structures (streaks) over smooth walls. However, they do push the near-wall structures upward allowing them to interact with the riblet tips. The resulting increase in spanwise friction at the wall restricts the spanwise movement of streamwise vortices (Choi *et al.* 1993; Jiménez & Pinelli 1999; Lee & Lee 2001) and, ultimately, weakens the quasi-streamwise vortices and reduces drag. On the other hand, larger riblets distort the streamwise streaks by increasing their lateral span from 52 viscous units above small riblets ($l_g^+ \approx 5$) to 57 viscous units above large ones ($l_g^+ \approx 20$); see figures 24(d) and 24(f). In the latter case, flow structures penetrate the riblet grooves (figure 24(f)), increasing drag by exposing a larger surface area to high-speed flow (Choi *et al.* 1993). The reduction in large-scale streamwise energy near the wall in the presence of riblets (figure 21) is attributed to the interaction between near-wall turbulence and the spanwise-periodic surface corrugation. This interaction induces secondary motions and amplifies

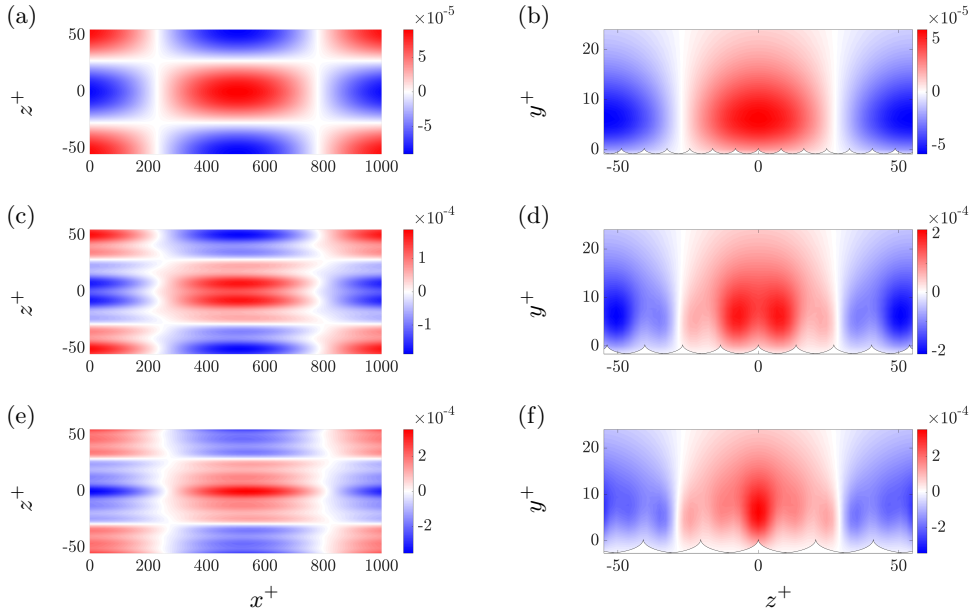


FIGURE 24. Dominant near-wall flow structures in turbulent channel flow with $Re_\tau = 547$ over semi-circular riblets with $\alpha/s = 0.55$ and (a,b) $l_g^+ \approx 5$ ($\omega_z = 460$); (c,d) $l_g^+ \approx 10$ ($\omega_z = 230$); (e,f) $l_g^+ \approx 20$ ($\omega_z = 115$). The first column shows the streamwise velocity u from the top view (x - z plane) one viscous unit above the crest of riblets, i.e., at (a) $y^+ \approx 2$, (c) $y^+ \approx 3$, and (e) $y^+ \approx 5$. The second column shows the same quantity from the cross-plane view (y - z plane) at $x^+ = 500$. Here, $(\lambda_x^+, \lambda_z^+) \approx (1100, 110)$ corresponds to typical scales of the near-wall cycle, which are extracted from the dominant eigenmode of the covariance matrix $\Phi_\theta(k_x)$.

cross-flow fluctuations in the vicinity of the riblets (Goldstein & Tuan 1998; Endrikat *et al.* 2022).

5.3. The absence of Kelvin-Helmholtz rollers over separated riblets

As demonstrated in § 5.1, large riblets generate spanwise rollers driven by the K-H instability. In this subsection, we analyze the spectral signature of these K-H rollers in the presence of separated semi-circular riblets. To achieve separation, we reduce the spanwise coverage of the semi-circular riblets within one period, creating periodic roughness elements separated by a spanwise distance of π/ω_z ; see figure 25. Figure 26 shows the effect of separated semi-circular riblets with $\alpha/s = 0.55$ and different sizes on the premultiplied wall-normal energy spectrum of channel flow with $Re_\tau = 934$ one viscous unit above the riblet crests. In contrast to large connected riblets that amplified the wall-normal energy in the spectral range corresponding to spanwise rollers (figure 13(c)), large separated riblets amplify the energy outside this range (figure 26(c)). Furthermore, separated riblets of small and optimal size suppress the wall-normal energy across all wavenumbers. In fact, regardless of their size, semi-circular riblets that are separated do not alter the energy of the wall-normal velocity in the K-H spectral region. This effect, which can be related to the penetration of turbulence in the riblet valleys, is in agreement with the findings of Endrikat *et al.* (2021).

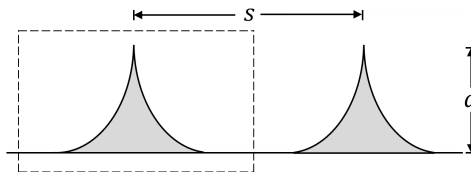


FIGURE 25. Separated semi-circular riblets of height α and peak to peak spacing s . The black dashed box delimits a $2\pi/\omega_z$ period of the riblets.

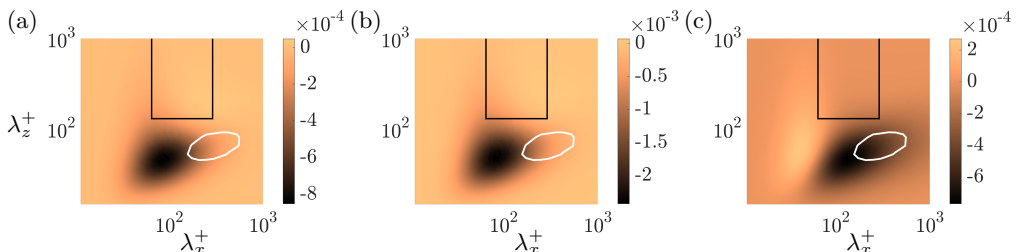


FIGURE 26. Premultiplied modifications to the wall-normal energy spectrum, $k_x k_z (\alpha E_{vv,1} + \alpha^2 E_{vv,2})$, of turbulent channel flow with $Re_\tau = 934$ above the crest of separated semi-circular riblets with $\alpha/s = 0.55$ and (a) $l_g^+ \approx 5$ ($\omega_z = 780$), (b) $l_g^+ \approx 10$ ($\omega_z = 390$), and (c) $l_g^+ \approx 20$ ($\omega_z = 200$). Black lines delimit the spectral window of K-H rollers and white solid lines correspond to the 80% contour level of the energy spectrum of smooth channel flow.

6. Concluding remarks

We develop a model-based framework for investigating the effects of surface corrugation, specifically semi-circular riblets, on skin-friction drag, kinetic energy, and flow mechanisms that lead to the break-down of the linear viscous regime in turbulent channel flow. Our approach combines the turbulence modeling technique adopted by Ran *et al.* (2021) with a domain transformation method that accurately represents corrugated surfaces. This approach uses the second-order statistics of velocity fluctuations to modify the turbulent eddy-viscosity of smooth channel flow. As the domain transformation reflects the spatial periodicity of the boundary conditions onto the differential operators, it significantly increases the computational complexity of the harmonic equations that need to be solved for the statistical response of the linearized dynamics. To manage this complexity, we introduce the riblet height as a small parameter, enabling a perturbation analysis of flow quantities. This approach breaks the dimensional complexity of the governing equations over smaller, more-manageable equations, facilitating the use of more collocation points near the surface of sharp riblets in high-Reynolds-number flows.

Our perturbation analysis enables the calculation of riblet-induced modifications to the second-order statistics and, thus, the energy spectrum of turbulent channel flows, capturing the effect of riblets on various spatial wavelengths. By employing an appropriate turbulence model, we extend this analysis to the turbulent viscosity and the mean velocity, from which skin-friction drag can be computed. Our framework's predictions closely align with drag-reduction trends reported by previous high-fidelity simulations and experiments. Furthermore, we analyze the primary flow mechanisms affecting drag reduction for large and sharp riblets. By examining riblet-induced changes to the energy spectrum, we assess how riblet size and height influence the amplification of K-H rollers at different Reynolds numbers. Our findings reveal that spectral evidence for these spanwise-coherent flow structures diminishes as the separation between roughness

elements increases. Finally, we explore the effect of large riblets in suppressing the energy of streaks close to the wall.

This work marks a significant step toward establishing a unified framework for low-complexity modeling of turbulent flows over rough surfaces. Our ongoing efforts are directed at leveraging this model-based framework to predict the impact of riblet erosion, such as tip roundness and height loss (Packard, Duetsch-Patel & Adjorlolo 2024), on the performance of maritime and ariel vehicles (Bilinsky *et al.* 2024). The integration of alternative turbulent viscosity models (e.g., Lasagna, Zampino & Ganapathisubramani (2024)), along with the incorporation of data from numerical simulations and experiments (e.g., Zare *et al.* (2017*a,b*, 2020)), can further enhance the predictive accuracy of our framework and playing a crucial role in broadening its applicability across various engineering applications.

Acknowledgments

Financial support from the Air Force Office of Scientific Research under award FA9550-23-1-0219 is gratefully acknowledged. The Office of Information Technology Cyberinfrastructure Research Computing (CIRC) at The University of Texas at Dallas and the Texas Advanced Computing Center are acknowledged for providing computing resources.

Declaration of Interests

The authors report no conflict of interest.

Appendix A. The operators \mathcal{A}_θ , \mathcal{B}_θ , and \mathcal{C}_θ in equations (3.6)

The dynamical generator matrix $\mathcal{A}_\theta(k_x)$ in evolution model (3.6) has the bi-infinite structure

$$\mathcal{A}_\theta(k_x) = \begin{bmatrix} \ddots & & & & & \ddots \\ \cdots & A_0(\theta_{n-1}) & A_{-1}(\theta_n) & A_{-2}(\theta_{n+1}) & \cdots & \\ \cdots & A_1(\theta_{n-1}) & A_0(\theta_n) & A_{-1}(\theta_{n+1}) & \cdots & \\ \cdots & A_2(\theta_{n-1}) & A_1(\theta_n) & A_0(\theta_{n+1}) & \cdots & \\ \ddots & & & & & \ddots \end{bmatrix}, \quad (\text{A } 1)$$

where the block operator $A_m(\theta_n)$ accounts for the influence of the $(m+n)$ th harmonic of the state, $\hat{\psi}_{m+n}$, on the dynamics of the n th harmonic of the state, $\hat{\psi}_n$. Each block operator takes the 2×2 form:

$$A_m(\theta_n) = \begin{bmatrix} A_{m,1,1}(k_x, \theta_n) & A_{m,1,2}(k_x, \theta_n) \\ A_{m,2,1}(k_x, \theta_n) & A_{m,2,2}(k_x, \theta_n) \end{bmatrix}.$$

For the block operator on the main diagonal of $\mathcal{A}_\theta(k_x)$ ($m = 0$),

$$\begin{aligned}
 A_{0,1,1}(k_x, \theta_n) &= \frac{\Delta_n^{-1}}{Re_\tau} \left[(1 + \nu_T) \Delta_n^2 + 2\nu_T'' \partial_{yy} - \nu_T'' \Delta_n + 2\nu_T' \Delta_n \partial_y \right] \\
 &\quad + \Delta_n^{-1} \left[ik_x (U_0'' - U_0 \Delta_n) \right] + \Gamma_{0,1,1}, \\
 A_{0,1,2}(k_x, \theta_n) &= \Gamma_{0,1,2}, \\
 A_{0,2,1}(k_x, \theta_n) &= -i\theta_n U_0' + \Gamma_{0,2,1}, \\
 A_{0,2,2}(k_x, \theta_n) &= \frac{1}{Re_\tau} [(1 + \nu_T) \Delta_n + \nu_T' \partial_y] - ik_x U_0 + \Gamma_{0,2,2},
 \end{aligned} \tag{A 2}$$

and otherwise ($m \neq 0$),

$$\begin{aligned}
 A_{m,1,1}(k_x, \theta_n) &= \Gamma_{m,1,1}, & A_{m,1,2}(k_x, \theta_n) &= \Gamma_{m,1,2}, \\
 A_{m,2,1}(k_x, \theta_n) &= \Gamma_{m,2,1}, & A_{m,2,2}(k_x, \theta_n) &= \Gamma_{m,2,2}.
 \end{aligned} \tag{A 3}$$

In equations (A 2) and (A 3),

$$\begin{aligned}
 \Gamma_{m,1,1} &= \frac{\Delta_n^{-1}}{Re_\tau} \left[F_m' (2\nu_T' \Delta_{m+n} \partial_y + 2\nu_T'' (\Delta_{m+n} + \partial_{yy}) - 2\nu_T''' \partial_{yy}) \right. \\
 &\quad \left. + F_m' ik_x (U_m'' + 2U_m' \partial_y) + ik_x (m^2 \omega_z^2 U_m - U_m \Delta_{m+n} - U_m'' \partial_y) \right], \\
 \Gamma_{m,1,2} &= \Delta_n^{-1} \left[2 \frac{m \omega_z k_x}{k_{m+n}^2} (F_m' F_m U_m'' + 2F_m' U_m' + 2F_m' F_m U_m' \partial_y + 2F_m' U_m \partial_y) \right], \\
 \Gamma_{m,2,1} &= -im \omega_z (F_m' F_m U_m' \partial_y + F_m' F_m U_m'' + F_m' U_m') - i\theta_{m+n} F_m' U_m' \\
 &\quad + \left[\frac{-im \omega_z}{k_x k_{m+n}^2} (iF_m^3 U_m' F_m' \partial_{yyy} - \theta_{m+n} F_m^2 U_m' F_m' \partial_{yy}) \right. \\
 &\quad \left. - m \omega_z F_m^2 U_m F_m' \partial_{yyy} - i\theta_{m+n} U_m m \omega_z F_m F_m' \partial_{yy} \right. \\
 &\quad \left. + iF_m^3 U_m'' F_m' \partial_{yy} - 2m \omega_z F_m^2 U_m' F_m' \partial_{yy} + im^2 \omega_z^2 U_m F_m F_m' \partial_{yy} \right. \\
 &\quad \left. - \frac{im \omega_z k_x^2}{k_{m+n}^2} (F_m U_m' (im \omega_z F_m \partial_y + i\theta_{m+n})^{-1} F_m' \partial_y \right. \\
 &\quad \left. + U_m (im \omega_z F_m \partial_y + i\theta_{m+n})^{-1} F_m' \partial_y) \right], \\
 \Gamma_{m,2,2} &= \frac{1}{Re_\tau} [(1 + \nu_T) \Delta_{m+n} + F_m'^2 \nu_T' \partial_y] - ik_x U_m + (im \omega_z F_m^2 U_m' \\
 &\quad - m^2 \omega_z^2 F_m U_m) \partial_y + \frac{m \omega_z}{k_{m+n}^2} (iF_m U_m' - \theta_{m+n} U_m \\
 &\quad + iF_m^2 U_m'' - 2im \omega_z F_m U_m' - m \omega_z U_m - iF_m U_m' + ik_x U_m),
 \end{aligned}$$

with $\theta_{m+n} = \theta + (m+n)\omega_z$, $k_{m+n}^2 = k_x^2 + \theta_{m+n}^2$, and $\Delta_{m+n} = F_m'^2 \partial_{yy} - k_{m+n}^2$.

The input and output matrices in equations (3.6) take the block diagonal forms $\mathcal{B}_\theta(k_x) = \text{diag} \{B(k_x, \theta_n)\}_{n \in \mathbb{Z}}$ and $\mathcal{C}_\theta(k_x) = \text{diag} \{C(k_x, \theta_n)\}_{n \in \mathbb{Z}}$, respectively, with

$$B(k_x, \theta_n) = \begin{bmatrix} B_v \\ B_\eta \end{bmatrix} = \begin{bmatrix} -ik_x \Delta_n^{-1} \partial_y & -ik_n^2 \Delta_n^{-1} & -i\theta_n \Delta_n^{-1} \partial_y \\ i\theta_n I & 0 & -ik_x I \end{bmatrix}, \tag{A 4}$$

and at higher levels of the perturbation series, the submatrices are given as

$$\begin{aligned}
 A_{l,m,1,1}(k_x, \theta_n) &= \frac{\Delta_{0,n}^{-1}}{Re_\tau} \left[F'_{l,m} (2\nu'_T \Delta_{0,n} \partial_y + 2\nu''_T (\Delta_{0,n} + \partial_{yy}) - 2\nu'''_T \partial_{yyy}) \right. \\
 &\quad \left. + ik_x (F'_{l,m} (U''_{l,m} + 2U'_{l,m} \partial_y) + m^2 \omega_z^2 U_{l,m} - U_{l,m} \Delta_{0,n} - U''_{l,m} \partial_y) \right], \\
 A_{l,m,1,2}(k_x, \theta_n) &= -\Delta_{0,n}^{-1} \left[2 \frac{m \omega_z k_x}{k_n^2} F'_{l,m} (F_{l,m} U''_{l,m} + 2U'_{l,m} + 2F_{l,m} U'_{l,m} \partial_y + 2U_{l,m} \partial_y) \right], \\
 A_{l,m,2,1}(k_x, \theta_n) &= -im \omega_z F'_{l,m} (F_{l,m} U'_{l,m} \partial_y + F_{l,m} U''_{l,m} + U'_{l,m}) - i\theta_n F'_{l,m} U'_{l,m} \\
 &\quad + \left[\frac{m \omega_z}{k_x k_n^2} F'_{l,m} F_{l,m} (F_{l,m}^2 U'_{l,m} \partial_{yyy} + i\theta_n F_{l,m} U'_{l,m} \partial_y) \right. \\
 &\quad + im \omega_z F_{l,m} U_{l,m} \partial_{yyy} - \theta_n U_{l,m} m \omega_z \partial_{yy} + F_{l,m}^2 U''_{l,m} \partial_{yy} \\
 &\quad \left. + 2im \omega_z F_{l,m} U'_{l,m} \partial_{yy} + m^2 \omega_z^2 U_{l,m} \partial_{yy} \right) \\
 &\quad - \frac{im \omega_z k_x^2}{k_n^2} (F'_{l,m} (im \omega_z F_{l,m} \partial_y + i\theta_n)^{-1} (F_{l,m} U'_{l,m} \partial_y + U_{l,m} \partial_y)) \Big], \\
 A_{l,m,2,2}(k_x, \theta_n) &= \frac{1}{Re_\tau} \left[(1 + \nu_T) \Delta_{0,n} + F_{l,m}^2 \nu'_T \partial_y \right] - ik_x U_{l,m} + \left(im \omega_z F_{l,m}^2 U'_{l,m} \right. \\
 &\quad \left. - m^2 \omega_z^2 F_{l,m} U_{l,m} \right) \partial_y + \frac{im \omega_z}{k_n^2} \left(F_{l,m} U'_{l,m} + i\theta_n U_{l,m} \right. \\
 &\quad \left. + F_{l,m}^2 U''_{l,m} - 2m \omega_z F_{l,m} U'_{l,m} + im \omega_z U_{l,m} - F_{l,m} U'_{l,m} + k_x U_{l,m} \right).
 \end{aligned}$$

Appendix C. Perturbation analysis of Lyapunov equation (3.7)

For $\alpha \ll 1$, Lyapunov equation (3.7) can be efficiently solved via perturbation analysis. Substituting (3.11) and (3.12) into (3.7) and collecting equal powers of α yields the sequence of Lyapunov equations,

$$\begin{aligned}
 \alpha^0: \quad \mathcal{A}_{0,\theta} \mathcal{X}_{0,\theta} + \mathcal{X}_{0,\theta} \mathcal{A}_{0,\theta}^* &= -\mathcal{M}_\theta \\
 \alpha^l: \quad \mathcal{A}_{0,\theta} \mathcal{X}_{l,\theta} + \mathcal{X}_{l,\theta} \mathcal{A}_{0,\theta}^* &= -\sum_{p=1}^l (\mathcal{A}_{p,\theta} \mathcal{X}_{l-p,\theta} + \mathcal{X}_{l-p,\theta} \mathcal{A}_{p,\theta}^*)
 \end{aligned} \tag{C1}$$

where the first subscript denotes the perturbation index and the dependence of operators $\mathcal{A}_{l,\theta}$, $\mathcal{X}_{l,\theta}$, and \mathcal{M}_θ on k_x is suppressed in favor of brevity. For the level of α^0 , we follow Moarref & Jovanovic (2012) and select the block-diagonal operator $\mathcal{M}_\theta(k_x)$ such that the energy spectrum of the stochastically forced linearized NS equations given by $\text{trace}(\mathcal{X}_{0,\theta}(k_x))$ matches that of a turbulent channel flow with smooth walls. This is done by scaling the block covariances of forcing as

$$\mathcal{M}(k_x, \theta_n) = \frac{\bar{E}_s(k_x, \theta_n)}{\bar{E}_{s,0}(k_x, \theta_n)} \mathcal{M}_s(k_x, \theta_n),$$

where, $\bar{E}_s(k_x, \theta_n) = \int_{-1}^1 E_s(y, k_x, \theta_n) dy$ is the two-dimensional energy spectrum of turbulent channel flow with smooth walls obtained from the DNS-based energy spectrum $E_s(y, k_x, \theta_n)$ (Del Álamo & Jiménez 2003), and $\bar{E}_{s,0}(k_x, \theta_n)$ is the energy spectrum resulting from the linearized NS equations (3.6) subject to white-in-time stochastic forcing with covariance matrix

$$\mathcal{M}_s(k_x, \theta_n) = \begin{bmatrix} \sqrt{E_s(y, k_x, \theta_n)} I & 0 \\ 0 & \sqrt{E_s(y, k_x, \theta_n)} I \end{bmatrix} \begin{bmatrix} \sqrt{E_s(y, k_x, \theta_n)} I & 0 \\ 0 & \sqrt{E_s(y, k_x, \theta_n)} I \end{bmatrix}^*$$

Alternative forcing models (e.g., (Zare *et al.* 2014, 2017*a,b*, 2020)) that may result in more accurate predictions of two-point correlations at the level of α^0 could also be used here. Due to the block-diagonal structure of $\mathcal{A}_{l,\theta}$ (equation (B 1)), the solution $\mathcal{X}_{l,\theta}$ inherits the structure of the right-hand side operator, i.e.,

$$\begin{aligned}\mathcal{X}_{0,\theta}(k_x) &= \text{diag} \{X_{0,0}(k_x, \theta_n)\} \\ \mathcal{X}_{l,\theta}(k_x) &= \text{Toep} \left\{ \cdots, X_{l,1}^*(k_x, \theta_n), \boxed{X_{l,0}(k_x, \theta_n)}, X_{l,1}(k_x, \theta_n), \cdots \right\}\end{aligned}$$

where the box denotes the element on the main diagonal of $\mathcal{X}_{l,\theta}$. Each block can be computed by substituting for $\mathcal{A}_{l,\theta}$ and $\mathcal{X}_{l,\theta}$ into equations (C 1) to obtain a coupled system of Lyapunov equations as shown below up to α^2 :

$$\begin{aligned}\alpha^0: \quad & A_{0,0}(\theta_n)X_{0,0}(\theta_n) + X_{0,0}(\theta_n)A_{0,0}^*(\theta_n) = -M(\theta_n) \\ \alpha^1: \quad & A_{0,0}(\theta_{n-m})X_{1,m}(\theta_n) + X_{1,m}(\theta_n)A_{0,0}^*(\theta_{n-m}) = -(A_{1,-m}(\theta_n)X_{0,0}(\theta_n) \\ & \quad \quad \quad + X_{0,0}(\theta_{n-m})A_{1,m}^*(\theta_{n-m})) \\ \alpha^2: \quad & A_{0,0}(\theta_n)X_{2,0}(\theta_n) + X_{2,0}(\theta_n)A_{0,0}^*(\theta_n) = -(A_{2,0}(\theta_n)X_{0,0}(\theta_n) + X_{0,0}(\theta_n)A_{2,0}^*(\theta_n) \\ & \quad \quad \quad + \sum_{m \in \mathbb{Z}} A_{1,m}(\theta_{n-m})X_{1,m}(\theta_n) \\ & \quad \quad \quad + \sum_{m \in \mathbb{Z}} X_{1,m}(\theta_n)A_{1,m}^*(\theta_{n-m})).\end{aligned}$$

Appendix D. Computing modifications at the level of α^1 and α^2 to k and ϵ in equations (3.14)

The average effect of velocity fluctuations on α^1 - and α^2 -level modifications to k and ϵ are obtained from autocorrelation operators $X_{1,0}(k_x, \theta_n)$ and $X_{2,0}(k_x, \theta_n)$, respectively, as

$$\begin{aligned}k_l(y) &= \int_0^\infty \int_0^{\omega_z} \sum_{n \in \mathbb{Z}} K_{l,k}(y, k_x, \theta_n) d\theta dk_x, \\ \epsilon_l(y) &= \int_0^\infty \int_0^{\omega_z} \sum_{n \in \mathbb{Z}} K_{l,\epsilon}(y, k_x, \theta_n) d\theta dk_x.\end{aligned}$$

Here, $K_{l,k}(y, k_x, \theta_n)$ and $K_{l,\epsilon}(y, k_x, \theta_n)$ are the kernel representation of operators $\mathcal{K}_{l,k}$ and $\mathcal{K}_{l,\epsilon}$, respectively, that can be computed from the central block (corresponding to the 0th harmonic) of solution $\mathcal{X}_{l,\theta}(k_x)$ of the respective Lyapunov equation at the l th perturbation level, i.e.,

$$\begin{aligned}\mathcal{K}_{l,k}(k_x, \theta_n) &= (C_u X_{l,0} C_u^* + C_v X_{l,0} C_v^* + C_w X_{l,0} C_w^*)/2, \\ \mathcal{K}_{l,\epsilon}(k_x, \theta_n) &= 2(k_x^2 C_u X_{l,0} C_u^* + \partial_y C_v X_{l,0} C_v^* \partial_y^* + \theta_n^2 C_w X_{l,0} C_w^* - ik_x \partial_y C_u X_{l,0} C_v^* \\ & \quad + k_x \theta_n C_u X_{l,0} C_w^* + i\theta_n C_v X_{l,0} C_w^* \partial_y^*) + \partial_y C_u X_{l,0} C_u^* \partial_y^* + k_x^2 C_v X_{l,0} C_v^* \\ & \quad + \partial_y C_w X_{l,0} C_w^* \partial_y^* + k_x^2 C_w X_{l,0} C_w^* + \theta_n^2 C_u X_{l,0} C_u^*\end{aligned}$$

where, C_u , C_v , and C_w are finite-dimensional representations of the output operators in appendix (A 5) and covariance matrices $X_{l,0}$ are confined to the wall-normal range $y \in [-1, 1]$ to provide appropriate comparison between the flows over smooth and corrugated surfaces. In figure 9(b), we retrieve the dependence of the turbulent kinetic energy on

the spanwise dimension via

$$k_l(y, z) = \int_0^\infty \int_0^{\omega_z} \sum_{n \in \mathbb{Z}} \operatorname{Re} (K_{l,k}(y, k_x, \theta_n) e^{ik_x x}) \cos(\theta_n z) d\theta dk_x.$$

Appendix E. Calculating the effect of fluctuations on the mean velocity and skin-friction drag

The effect of fluctuations on the mean velocity are realized through the riblet induced modifications to the turbulent viscosity. By substituting expansions (3.9), (3.10), and (3.15) into the mean flow equations (2.11), one can solve for zero-bulk perturbations to the mean velocity U_l via

$$U_l(y) = \bar{U}_{l,0}(y) - \bar{P}_{x,l} U_0(y)$$

where $\bar{U}_{l,0}$ ($l = 1$ and 2) are the 0th harmonics of the solution to the coupled equations

$$\begin{aligned} (1 + \nu_{T_0}) [\partial_{yy} + \partial_{zz}] \bar{U}_1 + \nu'_{T_0} \partial_y \bar{U}_1 &= -\partial_y (\nu_{T_1} \partial_y U_0) - 2F_{\bar{y}_1} \partial_y ((1 + \nu_{T_0}) \partial_y U_0) \\ (1 + \nu_{T_0}) [\partial_{yy} + \partial_{zz}] \bar{U}_2 + \nu'_{T_0} \partial_y \bar{U}_2 &= 2F_{\bar{z}_1} (1 + \nu_{T_0}) \partial_{yz} \bar{U}_1 - F_{\bar{z}_1}^2 \partial_y ((1 + \nu_{T_0}) \partial_y U_0) \\ &\quad - \partial_y (\nu_{T_1} \partial_y \bar{U}_1) - 2F_{\bar{y}_1} \partial_y ((1 + \nu_{T_0}) \partial_y \bar{U}_1) \\ &\quad - 2F_{\bar{y}_1} \partial_y (\nu_{T_1} \partial_y U_0) - \partial_y (\nu_{T_2} \partial_y U_0) \\ &\quad - (F_{\bar{y}_1}^2 + 2F_{\bar{y}_2}) \partial_y ((1 + \nu_{T_0}) \partial_y U_0) \end{aligned} \tag{E1}$$

and $\bar{P}_{x,l} = (\int_{-1-\alpha_p}^1 \bar{U}_{l,0}(y) dy) / (2U_B)$. We use 25 harmonics, i.e., $k = -12, \dots, 12$ in equation (2.13), to capture riblet-induced modifications to the mean velocity at both perturbation levels. The inclusion of a sufficient number of harmonics is ensured by evaluating the incremental effect of additional harmonics on the overall results.

REFERENCES

- ABOOTORABI, S. & ZARE, A. 2023 Model-based spectral coherence analysis. *J. Fluid Mech.* **958**, A16 (32 pages).
- AURENTZ, J. L. & TREFETHEN, L. N. 2017 Block operators and spectral discretizations. *SIAM Rev.* **59** (2), 423–446.
- BAKEWELL, H. P. & LUMLEY, J. L. 1967 Viscous sublayer and adjacent wall region in turbulent pipe flow. *Phys. Fluids* **10** (9), 1880–1889.
- BECHERT, D. W. & BARTENWERFER, M. 1989 The viscous flow on surfaces with longitudinal ribs. *J. Fluid Mech.* **206**, 105–129.
- BECHERT, D. W., BRUSE, M. & HAGE, W. 2000 Experiments with three-dimensional riblets as an idealized model of shark skin. *Experiments in fluids* **28** (5), 403–412.
- BECHERT, D. W., BRUSE, M., HAGE, W., VAN DER HOEVEN, J. G. T. & HOPPE, G. 1997 Experiments on drag-reducing surfaces and their optimization with an adjustable geometry. *J. Fluid Mech.* **338**, 59–87.
- BENSOUSSAN, A., LIONS, J. L. & PAPANICOLAOU, G. 1978 *Asymptotic Analysis for Periodic Structures*. North Holland.
- BILINSKY, H. C., BELL, D. C., SHYAM, D., WANG, G., BRISSON, E., QUINN, M. S. & MCGRATH, D. 2024 Growing riblets with light: Rapid prototyping of riblet designs, drag reduction analysis and product lifetime performance. In *AIAA SCITECH 2024 Forum*, p. 1110.
- BRUEGEM, W. P., BOERSMA, B. J. & UITTENBOGAARD, R. E. 2006 The influence of wall permeability on turbulent channel flow. *J. Fluid Mech.* **562**, 35–72.

- CABAL, A., SZUMBARSKI, J. & FLORYAN, J. M. 2002 Stability of flow in a wavy channel. *J. Fluid Mech.* **457**, 191–212.
- CESS, R. D. 1958 A survey of the literature on heat transfer in turbulent tube flow. *Westinghouse Research, Rep. 8-0529-R24*.
- CHAVARIN, A. & LUHAR, M. 2019 Resolvent analysis for turbulent channel flow with riblets. *AIAA Journal* pp. 1–11.
- CHOI, H., MOIN, P. & KIM, J. 1993 Direct numerical simulation of turbulent flow over riblets. *J. Fluid Mech.* **255**, 503–539.
- COUSTEIX, J. 1992 Basic concepts on boundary layers. *AGARD, Special Course on Skin Friction Drag Reduction*.
- DEAN, B. & BHUSHAN, B. 2010 Shark-skin surfaces for fluid-drag reduction in turbulent flow: a review. *Phil. Trans. R. Soc. A* **368** (1929), 4775–4806.
- DEL ÁLAMO, J. C. & JIMÉNEZ, J. 2003 Spectra of the very large anisotropic scales in turbulent channels. *Phys. Fluids* **15** (6), 41–44.
- DEL ÁLAMO, J. C. & JIMÉNEZ, J. 2006 Linear energy amplification in turbulent channels. *J. Fluid Mech.* **559**, 205–213.
- DEL ÁLAMO, J. C., JIMÉNEZ, J., ZANDONADE, P. & MOSER, R. D. 2004 Scaling of the energy spectra of turbulent channels. *J. Fluid Mech.* **500** (1), 135–144.
- VON DEYN, L.H., GATTI, D. & FROHNAPFEL, B. 2022 From drag-reducing riblets to drag-increasing ridges. *J. Fluid Mech.* **951**, A16.
- EHRENSTEIN, U. 1996 On the linear stability of channel flow over riblets. *Phys. Fluids* **8** (11), 3194–3196.
- ENDRIKAT, S., MODESTI, D., GARCÍA-MAYORAL, R., HUTCHINS, N. & CHUNG, D. 2021 Influence of riblet shapes on the occurrence of kelvin-helmholtz rollers. *J. Fluid Mech.* **913**, A37.
- ENDRIKAT, S., NEWTON, R., MODESTI, D., GARCÍA-MAYORAL, R., HUTCHINS, N. & CHUNG, D. 2022 Reorganisation of turbulence by large and spanwise-varying riblets. *J. Fluid Mech.* **952**, A27.
- FADLUN, E.A., VERZICCO, R., ORLANDI, P. & MOHD-YUSOF, J. 2000 Combined immersed-boundary finite-difference methods for three-dimensional complex flow simulations. *J. Comput. Phys.* **161**, 35–60.
- FARDAD, M., JOVANOVIĆ, M. R. & BAMIEH, B. 2008 Frequency analysis and norms of distributed spatially periodic systems. *IEEE Trans. Automat. Control* **53** (10), 2266–2279.
- FINNIGAN, J. 2000 Turbulence in plant canopies. *Annu. Rev. Fluid Mech.* **32**, 519–571.
- GARCÍA-MAYORAL, R. & JIMÉNEZ, J. 2011a Drag reduction by riblets. *Phil. Trans. R. Soc. A* **369** (1940), 1412–1427.
- GARCÍA-MAYORAL, R. & JIMÉNEZ, J. 2011b Hydrodynamic stability and breakdown of the viscous regime over riblets. *J. Fluid Mech.* **678**, 317–347.
- GARCÍA-MAYORAL, R. & JIMÉNEZ, J. 2012 Scaling of turbulent structures in riblet channels up to $Re_\tau \approx 550$. *Phys. Fluids* **24**, 105101.
- GOLDSTEIN, D., HANDLER, R. & SIROVICH, L. 1995 Direct numerical simulation of turbulent flow over a modelled riblet covered surface. *J. Fluid Mech.* **302**, 333–376.
- GOLDSTEIN, D.B. & TUAN, T.-C. 1998 Secondary flow induced by riblets. *J. Fluid Mech.* **363**, 115–151.
- HABIBI KHORASANI, S.M., LĀCIS, U., PASCHE, S., ROSTI, M.E. & BAGHERI, S. 2022 Near-wall turbulence alteration with the transpiration-resistance model. *J. Fluid Mech.* **942**, A45.
- HAMILTON, J. M., KIM, J. & WALEFFE, F. 1995 Regeneration mechanisms of near-wall turbulence structures. *J. Fluid Mech.* **287**, 317–348.
- HOYAS, S. & JIMÉNEZ, J. 2006 Scaling of the velocity fluctuations in turbulent channels up to $Re_\tau = 2003$. *Phys. Fluids* **18** (1), 011702.
- HUYNH, D. & MCKEON, B. J. 2020 Characterization of the spatio-temporal response of a turbulent boundary layer to dynamic roughness. *Flow Turbul. Combust.* **104** (2), 293–316.
- HWANG, Y. & BENGANA, Y. 2016 Self-sustaining process of minimal attached eddies in turbulent channel flow. *J. Fluid Mech.* **795**, 708–738.

- HWANG, Y. & COSSU, C. 2010 Linear non-normal energy amplification of harmonic and stochastic forcing in the turbulent channel flow. *J. Fluid Mech.* **664**, 51–73.
- IBRAHIM, I., DE SEGURA, G., GÓMEZ, CHUNG, D. & GARCÍA-MAYORAL, R. 2021 The smooth-wall-like behaviour of turbulence over drag-altering surfaces: a unifying virtual-origin framework. *J. Fluid Mech.* **915**, A56.
- JIMÉNEZ, J. 2013 Near-wall turbulence. *Phys. Fluids* **25** (10).
- JIMÉNEZ, JAVIER & PINELLI, ALFREDO 1999 The autonomous cycle of near-wall turbulence. *J. Fluid Mech.* **389**, 335–359.
- JIMENEZ, J., UHLMANN, M., PINELLI, A. & KAWAHARA, G. 2001 Turbulent shear flow over active and passive porous surfaces. *J. Fluid Mech.* **442**, 89–117.
- JONES, W.P. & LAUNDER, B.E. 1972 The prediction of laminarization with a two-equation model of turbulence. *Int. J. Heat Mass Transf.* **15** (2), 301–314.
- JOUIN, A., ROBINET, J.-C. & CHERUBINI, S. 2024 Modal and nonmodal stability of the laminar flow in a channel with longitudinal riblets. *Phys. Rev. Fluids* **9** (7), 073903.
- JOVANOVIĆ, M. R. 2020 From bypass transition to flow control and data-driven turbulence modeling: An input-output viewpoint. *Annu. Rev. Fluid Mech.* Submitted; also arXiv:2003.10104.
- JOVANOVIĆ, M. R. & BAMIEH, B. 2005 Componentwise energy amplification in channel flows. *J. Fluid Mech.* **534**, 145–183.
- KASLIWAL, A., DUNCAN, S. & PAPACHRISTODOULOU, A. 2012 Modelling channel flow over riblets: Calculating the energy amplification. In *Proceedings of 2012 UKACC International Conference on Control*, pp. 625–630.
- KHADRA, K., ANGOT, P., PARNEIX, S. & CALTAGIRONE, J. 2000 Fictitious domain approach for numerical modelling of Navier-Stokes equations. *Int. J. Numer. Methods Fluids* **34** (8), 651–684.
- LASAGNA, D., ZAMPINO, G. & GANAPATHISUBRAMANI, B. 2024 Linear models of strip-type roughness. *J. Fluid Mech.* **1001**, A38.
- LAUNDER, B.E. & SHARMA, B.I. 1974 Application of the energy-dissipation model of turbulence to the calculation of flow near a spinning disc. *Lett. Heat Mass Transf.* **1**, 131–137.
- LEE, S. J. & LEE, S.-H. 2001 Flow field analysis of a turbulent boundary layer over a riblet surface. *Experiments in fluids* **30** (2), 153–166.
- LUCHINI, P., MANZO, F. & POZZI, A. 1991 Resistance of a grooved surface to parallel flow and cross-flow. *J. Fluid Mech.* **228**, 87–109.
- MACDONALD, M., CHUNG, D., HUTCHINS, N., CHAN, L., OOI, A. & GARCÍA-MAYORAL, R. 2017 The minimal-span channel for rough-wall turbulent flows. *J. Fluid Mech.* **816**, 5–42.
- MCCOMB, W.D. 1991 *The Physics of Fluid Turbulence*. Oxford University Press.
- MITTAL, R., DONG, H., BOZKURTTAS, M., NAJJAR, F.M., VARGAS, A. & VON LOEBBECKE, A. 2008 A versatile sharp interface immersed boundary method for incompressible flows with complex boundaries. *J. Comput. Phys.* **227**, 4825–4852.
- MITTAL, R. & IACCARINO, G. 2005 Immersed boundary methods. *Annu. Rev. Fluid Mech.* **37**, 239–61.
- MOARREF, R. & JOVANOVIĆ, M. R. 2012 Model-based design of transverse wall oscillations for turbulent drag reduction. *J. Fluid Mech.* **707**, 205–240.
- MODESTI, D., ENDRIKAT, S., HUTCHINS, N. & CHUNG, D. 2021 Dispersive stresses in turbulent flow over riblets. *J. Fluid Mech.* **917**, A55.
- MOIN, P. & MOSER, R. D. 1989 Characteristic-eddy decomposition of turbulence in a channel. *J. Fluid Mech.* **200** (41), 509.
- MONTY, J. P., DOGAN, E., HANSON, R., SCARDINO, A. J., GANAPATHISUBRAMANI, B. & HUTCHINS, N. 2016 An assessment of the ship drag penalty arising from light calcareous tubeworm fouling. *Biofouling* **32** (4), 451–464.
- MORADI, H.V. & FLORYAN, J.M. 2014 Stability of flow in a channel with longitudinal grooves. *J. Fluid Mech.* **757**, 613–648.
- MORGAN, J. P. & MCKEON, B. J. 2018 Relation between a singly-periodic roughness geometry and spatio-temporal turbulence characteristics. *Int. J. Heat Fluid Flow* **71**, 322–333.
- NASERI, M. & ZARE, A. 2024 Model-based analysis of turbulent channel flow over riblets via change of coordinates. In *Proceedings of the 2024 AIAA Aviation Forum*, p. 3715 (13 pages).

- ODEH, F. & KELLER, J. B. 1964 Partial differential equations with periodic coefficients and Bloch waves in crystals. *J. Math. Phys.* **5**, 1499–1504.
- ORLANDI, P. & LEONARDI, S. 2006 DNS of turbulent channel flows with two- and three-dimensional roughness. *J. Turbul.* **7**, 1–22.
- PACKARD, N., DUETSCH-PATEL, J. & ADJOROLOLO, A. 2024 Development, testing and analysis of riblets for drag reduction. In *AIAA SCITECH 2024 Forum*, p. 1114.
- POPE, S. B. 2000 *Turbulent flows*. Cambridge University Press.
- PUJALS, G., GARCÍA-VILLALBA, M., COSSU, C. & DEPARDON, S. 2009 A note on optimal transient growth in turbulent channel flows. *Phys. Fluids* **21** (1), 015109.
- RAN, W., ZARE, A. & JOVANOVIĆ, M. R. 2021 Model-based design of riblets for turbulent drag reduction. *J. Fluid Mech.* **906**, A7 (38 pages).
- REYNOLDS, W. C. & HUSSAIN, A. 1972 The mechanics of an organized wave in turbulent shear flow. part 3. Theoretical models and comparisons with experiments. *J. Fluid Mech.* **54** (2), 263–288.
- REYNOLDS, W. C. & TIEDERMAN, W. G. 1967 Stability of turbulent channel flow with application to Malkus's theory. *J. Fluid Mech.* **27** (2), 253–272.
- ROUHI, A., ENDRIKAT, S., MODESTI, D., SANDBERG, R. D., ODA, T., TANIMOTO, K., HUTCHINS, N. & CHUNG, D. 2022 Riblet-generated flow mechanisms that lead to local breaking of Reynolds analogy. *J. Fluid Mech.* **951**, A45.
- SCHMID, P. J. & HENNINGSON, D. S. 2001 *Stability and Transition in Shear Flows*. New York: Springer-Verlag.
- SCHOPPA, W. & HUSSAIN, F. 2002 Coherent structure generation in near-wall turbulence. *J. Fluid Mech.* **453**, 57–108.
- DE SEGURA, G. GÓMEZ & GARCÍA-MAYORAL, R. 2019 Turbulent drag reduction by anisotropic permeable substrates – analysis and direct numerical simulations. *J. Fluid Mech.* **875**, 124–172.
- SHARMA, A. & GARCÍA-MAYORAL, R. 2020 Turbulent flows over dense filament canopies. *J. Fluid Mech.* **888**, A2.
- SPALART, P. R. & MCLEAN, J. D. 2011 Drag reduction: enticing turbulence, and then an industry. *Philos Trans A Math Phys Eng Sci.* **369**, 1556–1569.
- SUZUKI, Y. & KASAGI, N. 1994 Turbulent drag reduction mechanism above a riblet surface. *AIAA Journal* **32** (9), 1781–1790.
- VERZICCO, R. 2023 Immersed boundary methods: Historical perspective and future outlook. *Annu. Rev. Fluid Mech* **55**, 129–155.
- VIGGIANO, B., CAMOBRECO, C. J., WONG, J., LUHAR, M., GARCÍA-MAYORAL, R., CHUNG, D. & GAYME, D. 2024 The role of nonlinear interactions in the onset of drag increase in flow over riblets. *J. Phys. Conf. Ser* **2753**, 012010.
- WALSH, M. 1982 Turbulent boundary layer drag reduction using riblets. In *20th aerospace sciences meeting*, p. 169.
- WALSH, M. & LINDEMANN, A. 1984 Optimization and application of riblets for turbulent drag reduction. In *22nd Aerospace Sciences Meeting*, p. 347.
- WEIDEMAN, J. A. C. & REDDY, S. C. 2000 A MATLAB differentiation matrix suite. *ACM T. Math. Software* **26** (4), 465–519.
- WONG, J., CAMOBRECO, C.J., GARCÍA-MAYORAL, R., HUTCHINS, N. & CHUNG, D. 2024 A viscous vortex model for predicting the drag reduction of riblet surfaces. *J. Fluid Mech.* **978**, A18.
- ZARE, A., CHEN, Y., JOVANOVIĆ, M. R. & GEORGIU, T. T. 2017a Low-complexity modeling of partially available second-order statistics: theory and an efficient matrix completion algorithm. *IEEE Trans. Automat. Control* **62** (3), 1368–1383.
- ZARE, A., GEORGIU, T. T. & JOVANOVIĆ, M. R. 2020 Stochastic dynamical modeling of turbulent flows. *Annu. Rev. Control Robot. Auton. Syst.* **3**, 195–219.
- ZARE, A., JOVANOVIĆ, M. R. & GEORGIU, T. T. 2014 Completion of partially known turbulent flow statistics. In *Proceedings of the 2014 American Control Conference*, pp. 1680–1685.
- ZARE, A., JOVANOVIĆ, M. R. & GEORGIU, T. T. 2017b Colour of turbulence. *J. Fluid Mech.* **812**, 636–680.